The effect of Si and Y additives on the phase stability of Al_2O_3 thin films

Von der Fakultät für Georessourcen und Materialtechnik
der Rheinisch-Westfälischen Technischen Hochschule Aachen

zur Erlangung des akademischen Grades eines

Doktors der Ingenieurwissenschaften

genehmigte Dissertation

vorgelegt von **Dipl.-Ing.**

Farwah Nahif

aus Kabul, Afghanistan

Berichter: Univ.-Prof. Jochen M. Schneider, Ph.D.
Univ.-Prof. Dipl.-Ing. Dr. mont. Christian Mitterer

Tag der mündlichen Prüfung: 05. Dezember 2013

Materials Chemistry Dissertation

No.: 23 (2014)

Farwah Nahif

The effect of Si and Y additives on the phase stability of Al_2O_3 thin films

Shaker Verlag
Aachen 2014

Bibliographic information published by the Deutsche Nationalbibliothek
The Deutsche Nationalbibliothek lists this publication in the Deutsche Nationalbibliografie; detailed bibliographic data are available in the Internet at http://dnb.d-nb.de.

Zugl.: D 82 (Diss. RWTH Aachen University, 2013)

Printed in Germany.

ISBN 978-3-8440-2495-1
ISSN 1861-0595

Shaker Verlag GmbH • P.O. BOX 101818 • D-52018 Aachen
Phone: 0049/2407/9596-0 • Telefax: 0049/2407/9596-9
Internet: www.shaker.de • e-mail: info@shaker.de

„Bring vor, was wahr ist;
schreib so, dass es klar ist.
Und verficht's, bis es mit dir gar ist!"

Ludwig E. Boltzmann

Abstract

In this thesis, the effect of Si and Y alloying on the phase stability of Al_2O_3 polymorphs was investigated by ab initio calculations and experimental approach.

In the first part the effect of Si alloying on the phase stability of Al_2O_3 polymorphs has been studied. Using density functional theory, the effect of Si on the stability and electronic structure of γ- and α-Al_2O_3 has been investigated. The concentration range from 0 to 5 at.% is probed and the additive is positioned at different substitutional sites in the γ-phase. The calculations for $(Al,Si)_2O_3$ predict a trend towards spontaneous decomposition into α-/γ-Al_2O_3 and SiO_2. Therefore, the formation of the metastable γ-$(Al,Si)_2O_3$ phase can only be expected during non-equilibrium processing where the decomposition is kinetically hindered. The Si-induced changes in stability of this metastable solid solution may be understood based on the electronic structure. As the Si concentration is increased, stiff silicon–oxygen bonds are formed giving rise to the observed stabilization of the γ-phase. The effect of Si alloying on the phase transformation sequence and phase formation temperatures of Al_2O_3 thin films deposited by filtered cathodic arc was investigated by annealing experiments in air. By addition of Si the transformation of γ- to δ- and θ-Al_2O_3 is restrained by 100°C. The thermal stability range of the δ- and θ-phase is also increased by ≥ 200°C with respect to the unalloyed Al_2O_3 thin film and the formation of α-Al_2O_3 is restrained by 200°C upon addition of Si. Based on the here observed Si addition induced changes in phase formation, crystallite size and bonding it appears reasonable that the presence of SiO_2 at the grain boundaries impeding mass transport governs the Si induced stability enhancement of the metastable γ-/ δ- and θ-Al_2O_3 phases and the restrained α-Al_2O_3 formation. The competing proposal assuming a random substitution of Al by Si on the lattice sites is not consistent with the XPS data.

In the second part of the thesis the effect of 0.6 to 7.5 at.-% Y addition on the stability of Al_2O_3 has been investigated using density functional theory and post-annealing of Y alloyed alumina thin films deposited by filtered cathodic arc. The calculations indicate decomposition of the Y alloyed γ- and α-Al_2O_3 solid solutions into Y_2O_3 and the corresponding alumina phase. This prediction is consistent with experiments: The lattice parameters of the unalloyed and Y alloyed γ-Al_2O_3 thin films are comparable and are hence inconsistent with the predicted expansion in equilibrium volume as Y is incorporated into the γ-phase. The metastable character of γ-$(Al,Y)_2O_3$ is also consistent with the formation of γ-Al_2O_3, Y_2O_3, and $Y_3Al_5O_{12}$ in the as-deposited state as identified by X-ray diffraction. While the phase transition from the unalloyed γ-Al_2O_3 to α-Al_2O_3 phase takes place at 1000°C, it is restrained to 1200°C for the Y alloyed alumina thin films and additional formation of $YAlO_3$ and $Y_3Al_5O_{12}$ is observed. The by 100 °C $\leq$ T $\leq$ 200 °C restrained transition of the metastable γ-Al_2O_3 polymorph to α-Al_2O_3 may be explained by the segregation of Y at the metastable Al_2O_3 grain boundaries impeding mass transport and hence retard both grain growth of α-Al_2O_3 and α-Al_2O_3 formation.

Furthermore, Al_2O_3 thin films with 1.9 to 7 at.-% Y addition deposited by filtered cathodic arc technique at 650°C substrate temperature and -130 V bipolar pulsed dc substrate bias have been investigated regarding phase formation. Based on X-ray diffraction and transmission electron microscopy the formation of $YAlO_3$ and $Y_3Al_5O_{12}$ at Y concentrations ≥ 1.9 at.-% was observed in an amorphous matrix. The formation of yttrium aluminate precipitates at 650 °C underlines the potential of synthesis techniques utilizing ion bombardment of the film forming species for low temperature synthesis as the reported synthesis temperature for the bulk synthesis is 1600°C.

Zusammenfassung

Im Rahmen dieser Arbeit wurde der Einfluss von Si und Y Legierung auf die Phasenstabilität von Al_2O_3 Polymorphen anhand von ab initio Berechnungen und Experimenten untersucht.

Der erste Teil der Arbeit befasst sich mit der Untersuchung des Einflusses von Si-Additiven auf die Phasenstabilität von Al_2O_3 Polymorphen. Unter Einsatz der Dichtefunktionaltheorie wurde der Effekt von 0 bis 5 at.-% Si auf die Stabilität und die elektronische Struktur von γ- and α-Al_2O_3 untersucht. Die Al-Kationen in der γ- and α-Al_2O_3 Phase wurden dabei durch die entsprechende Anzahl Si-Kationen ersetzt. Innerhalb der γ-Phase wurden die Si-Kationen sowohl auf tetraedrischen als auch oktaedrischen Gitterplätzen angeordnet. Die Berechnungen für $(Al,Si)_2O_3$ prognostizieren eine spontanen Entmischung in α-/γ-Al_2O_3 and SiO_2. Daher ist die Bildung einer metastabilen γ-$(Al,Si)_2O_3$ nur während eines Nicht-Gleichgewichts-Prozesses, wenn die Entmischung kinetisch gehindert ist, zu erwarten. Die Si-induzierten Stabilitätsänderungen der Mischphase können basierend auf der elektronischen Struktur verstanden werden: Eine Erhöhung der Si-Konzentration führt zu der Bildung von steifen Si-O Bindungen, die somit zu der beobachteten Stabilität der γ-Phase führen. Darüber hinaus wurde der Effekt von Si-Additiven auf die Phasenumwandlung und Umwandlungstemperaturen von Al_2O_3 Dünnschichten welche mittels des gefilterten Lichtbogenverfahrens synthetisiert wurden, anhand von Heizversuchen, untersucht. Durch den Zusatz von Si wurde die Umwandlung von γ- zu δ- und θ-Al_2O_3 um 100°C verzögert. Die thermische Stabilität der δ- and θ-Phasen wurde, im Vergleich zu den unlegierten Al_2O_3 Dünnschichten um ≥ 200°C erhöht und die Bildung von α-Al_2O_3 um 200°C verzögert. Basierend auf den, durch die Si-Zugabe, beobachteten Änderungen in der Phasenbildung, Kristallitgröße und Bindungszuständen erscheint es wahrscheinlich, daß die Si-induzierte Stabilitätserhöhung der metastabilen γ-/

δ- and θ-Al_2O_3 Phasen und die verzögerte α-Al_2O_3 Bildung durch die Seigerung von SiO_2 an den Korngrenzen zu erklären ist. Eine substituierende Einbindung von Si auf Al-Gitterplätzen in der Al_2O_3 Struktur erscheint anhand der gelieferten XPS Ergebnisse unwahrscheinlich.

Im zweiten Teil der Arbeit wurde der Einfluss von 0.6 bis 7.5 at.-% Y anhand von Dichtefunktionaltheorie und Heizexperimenten auf die Stabilität und die Morphologie von Al_2O_3 Dünnschichten untersucht. Die Berechnungsergebnisse deuten eine spontane Entmischung der Y legierten γ- and α-Al_2O_3 Mischung in Y_2O_3 und den entsprechenden Alumina-Phasen an. Diese Prognose stimmt mit der experimentellen Beobachtung überein: Die Gitterparameter der unlegierten und Y legierten γ-Al_2O_3 Dünnschichten sind vergleichbar und weisen somit keine Übereinstimmung mit der, für die Einbindung von Y in die γ-Phase, prognostizierten Expansion des Gleichgewichtsvolumens auf. Der metastabile Charakter von γ-$(Al,Y)_2O_3$ stimmt darüber hinaus mit der, anhand von Röntgendiffraktometrie identifizierten Bildung von γ-Al_2O_3, Y_2O_3, und $Y_3Al_5O_{12}$ im abgeschiedenen Zustand überein. Während die Phasenumwandlung der unlegierten γ-Al_2O_3 zu α-Al_2O_3 Phase bei 1000°C stattfindet, wird die γ- zu α-Al_2O_3 Phasenumwandlung für Y legierten Alumina-Dünnschichten bis 1200°C verzögert und eine zusätzliche Bildung von $YAlO_3$ und $Y_3Al_5O_{12}$ beobachtet. Die, um 100 °C ≤ T ≤ 200 °C verzögerte γ- zu α-Al_2O_3 Phasenumwandlung kann anhand von Y Seigerungen entlang der metastabilen Al_2O_3 Korngrenzen erklärt werden, wodurch Massentransport gehemmt wird und somit Kornwachstum und die α-Al_2O_3 Bildung verzögert werden.

Darüber hinaus wurde die Phasenbildung von 1.9 bis 7 at.-% Y legierten Al_2O_3 Dünnschichten untersucht, die mittels gefiltertem Lichtbogenverfahrens bei einer Substrattemperatur von 650°C und einer bipolar gepulsten DC- Substratvorspannung von - 130 V synthetisiert wurden. Anhand von Röntgendiffraktometrie und Transmissions-

Elektronen-Mikroskopie-Analyse wurde die Bildung von $YAlO_3$ and $Y_3Al_5O_{12}$ innerhalb einer amorphen Matrix für Y Konzentrationen ≥ 1.9 at.-% beobachtet. Die Bildung dieser Yttriumaluminat-Ausfällung bei 650 °C verdeutlicht das Potential von Synthesetechniken, basierend auf Ionenbeschuss durch die schichtbildenden Spezies, für die Niedrig-Temperatur-Synthese von Yttriumaluminat-Phasen, deren Bulk-Synthese üblicherweise bei 1600°C beobachtet wird.

Preface

The work presented in this thesis is a part of the project funded by the Deutsche Forschungsgemeinschaft (DFG) within the project Schn 735/14-2 “Nanokristalline γ-Al_2O_3 Schichten”.

Publications

The following papers contributed to this thesis:

Paper I

Ab initio study of the effect of Si on the phase stability and electronic structure of γ- and α-Al_2O_3

F. Nahif, D. Music, S. Mráz, M. to Baben and J. M. Schneider

Journal of Physics: Condensed Matter 25 (2013) 125502

Paper II

The effect of Si alloying on the thermal stability of Al_2O_3 films deposited by filtered cathodic arc

F. Nahif, D. Music, S. Mráz, H. Bolvardi, L. Conrads and J. M. Schneider

Surface and Coatings Technology 235 (2013) 250–258

Paper III

Ab initio and experimental study on the effect of Y alloying on the phase stability of Al_2O_3 thin films deposited by filtered cathodic arc

F. Nahif, S. Mráz, D. Music, P. Keuter, J. M. Schneider

In manuscript

Paper IV

Low temperature synthesis of $Y_3Al_5O_{12}$ by using filtered cathodic arc technique

F.Nahif, M. G. J. Müller, S. Mráz, D. Music, J. Mayer, J. M. Schneider

In manuscript

Other Papers:

Bimodal substrate biasing to control γ-Al_2O_3 deposition during reactive magnetron sputtering

M. Prenzel, A. Kortmann, A. Stein, A. von Keudell, F. Nahif, J. M. Schneider

J. Appl. Phys. 114, (2013) 113301

Formation of crystalline γ-Al_2O_3 induced by variable substrate biasing during reactive magnetron sputtering

M. Prenzel, A. Kortmann, A. Keudell, F. Nahif, J. M. Schneider, M. Shihab, R. P. Brinkmann

Journal of Physics D: Appl. Phys. 46 (2013) 084004

Ab initio molecular dynamics of Al irradiation-induced processes during Al_2O_3 growth

D. Music, F. Nahif, K. Sarakinos, N. Friederichsen, J. M. Schneider

Appl. Phys. Lett. 98 (2011) 111908

Adaptive VN/Ag nanocomposite coatings with lubricious behavior from 25 to 1000 °C

S. M. Aouadi, D. P. Singh, D. S. Stone, K. Polychronopoulou, F. Nahif, C. Rebholz, C. Muratore, A . A. Voevodin

Acta Materialia 58 (2010) 5326–5331

On the phase formation of sputtered hafnium oxide and oxynitride films

K. Sarakinos, S. Mráz, K. Jiang, F. Nahif, A. Braun, C. Zilkens, S. Konstantinidis, F. Renaux, D. Cossement, F. Munnik, J. M. Schneider

J. Appl. Phys. 108 (2010) 014904

Ionized physical vapor deposited Al_2O_3 films: Does subplantation favor formation of α-Al_2O_3?

K. Sarakinos, F. Nahif, K. Jiang, A. Braun, C. Zilkens, J. M. Schneider

Phys. Status Solidi (Rapid Research Letter) 4 (2010) 154-156

Acknowledgements

Zu Beginn richtet sich mein ganz besonderer Dank an meinen Doktorvater Prof. Jochen M. Schneider, dafür, dass er mir die Möglichkeit gegeben hat meine Promotion am Lehrstuhl für Werkstoffchemie durchführen zu können und bereits während meines Studiums mein Interesse für die Dünnschicht-Technologie geweckt hat. Ich danke dir, Jochen, für dein Vertrauen in mich und meine Fähigkeiten und dafür, dass du meine Arbeit während der letzten vier Jahre durch inspirierende und motivierende Fachdiskussionen bereichert und unterstützt hast. Nicht weniger zu danken gilt es Prof. Christian Mitterer, für die Übernahme des Zweitgutachtens und dafür, dass er gemeinsam mit Prof. Jochen M. Schneider stets meine fachliche und berufliche Weiterentwicklung gefördert hat.

Des Weiteren möchte ich mich bei meinen wunderbaren Kollegen/-innen bedanken. Ein ganz besonderer und großer Dank richtet sich an Denis, Stano, Tetsuya und Moritz. Denis, danke dafür, dass du mich auf meiner Reise durch die unendlichen Weiten der ab initio Berechnungen begleitet hast. Deine jederzeit offene Tür, dein fachlicher Rat, sowie deine stets positive Art haben wesentlich zu meiner Doktorarbeit beigetragen und mich jederzeit aufs Neue motiviert. Stano und Tetsuya, auch euch danke ich vielmals für den inspirierenden Austausch an Ideen und das Wissen über die Vakuumtechnologie und die Plasmaphysik, das ihr in den vergangenen Jahren an mich weitergegeben habt. Danke auch an Moritz, für die interessanten fachlichen Gespräche, sowie dafür, dass du während der vergangenen Jahre mein Interesse für die Alchemie und den Fußball geweckt hast. Des Weiteren bin ich Herrn Horbach, Herrn Kaiser, Herrn Bohmke, Bernd, Stephan und Markus zu tiefem Dank verpflichtet. Diese Arbeit wäre nie zustanden gekommen ohne ihre bereitwillige Unterstützung bei Reparaturen und Umbauarbeiten an der Arc-Anlage. Ich danke ihnen für alles, was ich durch sie in den letzten vier Jahren gelernt habe.

Ein großer Dank richtet sich auch an meine Bürokollegen/-innen Carolin und Volker, dafür, dass der Arbeitstag durch ihre Anwesenheit und ihr fröhliches Wesen immer bereichert wurde und die immer ein offenes Ohr hatten, auch für Belange die über das Wissenschaftliche hinausgingen. Einen lieben Dank auch an meine weiteren Kollegen, die mich während meiner Doktorarbeit in organisatorischen und administrativen Belangen unterstützt und freundschaftlich begleitet haben: Michaela, Gabi, Marianne, Simon, Marcus, Stephanie, Yan, Lin, Thomas G., Jens, Kostas, Kaiyun, Hamid, Oliver, Friederike, Keke, Kalpak, Junaid, Yen-Ting, Laura, Phillip, Richard, Leo, Stephan und Niklas.

Ich danke euch für die warmherzige und kollegiale Arbeitsatmosphäre und es war mir eine Ehre mit euch allen zusammen arbeiten zu dürfen!

Meinen Kollegen innerhalb des DFG Projektes „Nanokristalline γ-Al_2O_3 Schichten", insbesondere Prof. Mayer und Merle Müller, danke ich sehr herzlich für die gute Zusammenarbeit.

Darüber hinaus möchte ich meinen Freunden danken, dafür, dass sie mich während meiner Promotion mit Geduld und der nötigen Ablenkung vom Wissenschaftsalltag begleitet haben.

Mein größter und eigentlich in Worten nicht erfassbarer Dank geht an meine Familie. An meinen Vater, Prof. Dr. A. A. Nahif, meiner Mutter Sheima Nahif und meine Schwester Yassnah Nahif. Ich danke euch von ganzem Herzen dafür, dass ihr immer an mich geglaubt und mir diesen Weg ermöglicht habt. Eurer stets ermutigenden Unterstützung und bedingungslosen Liebe in den letzten vier Jahren ist es zu verdanken, dass diese Doktorarbeit zustanden gekommen ist und daher sei die vorliegende Arbeit euch gewidmet.

TABLE OF CONTENTS

1. Introduction and Outline

Alumina (Al_2O_3) thin films synthesized by physical or chemical methods have been used for a variety of applications because of their outstanding properties. Crystalline Al_2O_3 thin films are used as dielectric in semiconductor devices [1], as passivation layer for organic light-emitting diodes [2] and in crystalline silicon solar cell because of their high dielectric constant and wide band gap [3]. Extensive applications in other industrial areas include wear and corrosion-resistance coatings [4] - [6]. Amorphous Al_2O_3 thin films are discussed as a potential alternative for SiO_2 as complementary metal-oxide-semiconductor transistor gate dielectric (CMOS), which demands a high thermodynamic stability and interface quality [7]. Furthermore amorphous alumina coatings are employed as heat and electrically insulating coatings for W-Ta-thin thermocouples [8] and magnetohydrodynamic (MHD) generators [9].

Besides the thermodynamically stable α-phase (space group $R\bar{3}c$, corundum), Al_2O_3 exhibits different polymorphs with various structures and properties such as the metastable γ-, δ-, and θ-phases. These metastable transition aluminas are widely used as catalyst in chemical processes because of their catalytic activity and high surface area [9] - [11]. While α-Al_2O_3 coatings have been applied in surface protection of cutting tools for many years, most of the commercial products are chemical vapor deposited [6], [12] on Cemented Carbide substrates. Although the thermodynamically stable α-Al_2O_3 is often used for applications at high thermal and mechanical load, the required deposition temperature in excess of 1000°C [13] limits the use of available substrate materials. During the mid 90's synthesis pathways for low temperature crystalline alumina were

investigated by [14], [15]. Most published alumina growth data suggest that ionized [16] and energetic [17] - [19] film forming species are prerequisites for crystalline growth at low temperatures. Besides the thermodynamically stable α-Al_2O_3 phase also the metastable γ-Al_2O_3 (space group $Fd\bar{3}m$) has been investigated as a potential alternative for wear resistant applications [20]. However, due to its metastable nature, PVD deposited [20] γ-Al_2O_3 transforms to the α-Al_2O_3 phase. According to high temperature XRD data reported by Trinh et al. the transformation occurs in the range of 950 – 975°C [21], which restricts the applicability of γ-Al_2O_3 coatings to temperatures lower than 950°C. Since this transformation is accompanied by a 14% decrease of volume [22], cohesive and/or adhesive failure may be caused by the stresses generated during the phase transformation. Thus, identifying strategies to restrain phase transformations is a key challenge to be addressed for extending the application temperature range of metastable alumina polymorphs. In this context the addition of alloying elements such as Er [23], La [24], Sr [25] and Y [23] on the thermal stability of alumina polymorphs has been investigated. The effect of Si and Y additions on the stability of alumina polymorphs was investigated by ab initio and experimentally in the past [26] - [28]. Although these studies addressed some major questions concerning the effects of additives on the relative stability of γ-$Al_2O_3$with respect to α-Al_2O_3, the underlying mechanisms driving the observed retardation of phase transitions are not fully understood.

The goal of this thesis is to understand the atomistic mechanisms governing the structure evolution to control or affect phase formation and stability of alumina thin films deposited by filtered cathodic arc technique. The thesis is, therefore, subdivided into five chapters:

A state of the art review is provided in Chapter 2. The review focuses on the polymorphism of alumina and the synthesis pathways for the different alumina polymorphs. Furthermore, it includes a summary of the current studies on the effect of additives on the stability of the metastable alumina phases with focus on the additives Si and Y. Chapter 3 describes the experimental and theoretical methods of research used within this study. Chapter 4 contains the experimental and theoretical studies of the effect of Si and Y additives on the high temperature stability of metastable γ-Al_2O_3. Chapter 5 concludes the thesis and future research directions and perspectives are proposed in Chapter 6.

2. State of the art

2.1 Alumina polymorphs and properties

Aside the formation of the thermodynamically stable α-Al_2O_3 phase, the synthesis of alumina by vapour deposition techniques includes the formation of several intermediate metastable phases, such as the γ-, δ-, θ- and κ-Al_2O_3 phase [29]. In general, the sequence of the metastable to thermodynamically stable α-Al_2O_3 phase transition is governed by temperature, as shown in Fig. 1. The following section gives a short description of the thermodynamically stable α-Al_2O_3 phase and the metastable alumina phases.

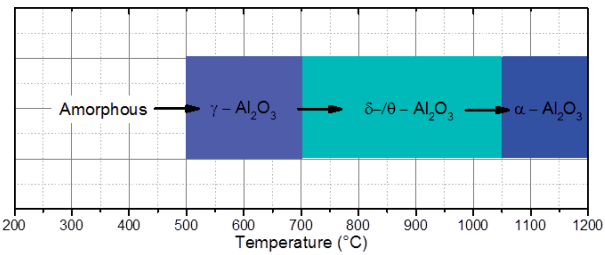

Fig. 1: PVD transition temperatures for selected alumina phases [29].

2.1.1 α-Al_2O_3

The thermodynamically stable α-Al_2O_3 phase (also known as corundum or sapphire) exhibits a rhombohedral structure (space group $R\bar{3}c$). However, it is conventionally described by a hexagonal closed packed (hcp) structure of oxygen anions where the aluminum cations occupy two third of the octahedral sites in the oxygen lattice. The lattice

parameter of the rhombohedral description are a = 5.128 Å and α = 55.3° [30]. The hexagonal cell exhibits lattice parameter of a = 4.76 Å and c = 12.99 Å [30]. Aside the thermal stability of the α-Al_2O_3 phase, which makes it a suitable coating material for high temperature applications [13], the α-Al_2O_3 phase exhibits a high hardness [31], chemical inertness [32] and good wear resistance [14]. Owing to these properties α-Al_2O_3 thin films are widely used as, e.g. insulating layers for semiconductor devices [33], wear resistant coatings for cutting tools [14] and as diffusion barrier coatings for turbine blades [34]. Table 1 summarizes selected properties of the thermodynamically stable α-phase.

Property	Value
Melting Point (°C)	2050 [35]
Density (g/cm³)	3.96 [29]
Elastic Modulus (GPa)	409 – 441 [31], [35]
Bulk Modulus (GPa)	239 [36]
Hardness (GPa)	28 [31]
Relative dielectric constant	10.6 [37]
Oxygen diffusivity (m^2/s)	10^{-21} to 10^{-24} [38], [39]

Table 1: Properties of α-Al_2O_3 at room temperature.

2.1.2 Metastable alumina phases

The most relevant metastable alumina phases, such as γ-, δ-, θ-Al_2O_3 exhibit face-centered cubic (fcc) packing of the oxygen anions while the κ-Al_2O_3 phase is described by a hcp arrangement of the oxygen sublattice. However, the exact structure of the γ-phase is not defined and has been extensively debated in the past. One structural proposal of γ-Al_2O_3 is a defect spinel (space group $Fd\bar{3}m$) with oxygen anions forming an fcc lattice while

the octahedral and tetrahedral sites are occupied by Al cations [40] - [42]. Within the framework of optimizing the spinel-based models, Paglia et al. [43] suggested that the occupation of non-spinel sites is energetically favorable compared to the spinel site occupation. These authors then proposed a tetragonal model, where the cations occupy the non-spinel c-symmetry sites (vacant sites in the spinel structure) and which provides good agreement with neutron diffraction pattern of the γ-Al_2O_3 phase [43]. Furthermore, Menéndez-Proupin et al. [44] studied the electronic structure of γ-Al_2O_3, by comparing the spinel model and the non-spinel model reported by Paglia et al. [40], [43]. In the scope of this study Menéndez-Proupin et al. [44] reported a by 5 meV/atom larger total energy for the non-spinel configuration than for the spinel configuration which is contradictive to the results of Paglia et al. [43] where the structure with non-spinel site occupancy was reported to be more energetically favorable. Furthermore, a comparison of the spinel configuration employed by Gutiérrez et al. [42] and tetragonal hausmannite structure based on reports of Knaup et al. [45] was performed by Jiang et al. [27]. With an energy difference of - 8 meV/atom with respect to the spinel configuration, the authors [27] reported the tetragonal hausmannite structure as suitable description of the γ-Al_2O_3 structure. However, the results obtained by theoretical approach are inconclusive as no generally valid description of the γ-Al_2O_3 structure has been introduced by now. While generally the combination of computational modeling and experimental analysis is accepted as promising strategy for structure determination, this is challenging for γ-Al_2O_3 as no single crystals can be obtained. Furthermore, the diffuse nature of the experimentally obtained γ-Al_2O_3 diffraction data (from polycrystals) as well as the concurrent presence of the γ-/δ-/θ-Al_2O_3 phases aggravates the verification of experimental results by simulated

diffraction data. In addition, computational modeling of complex structures like γ-Al_2O_3 involve the use of supercell configurations with larger number of atoms and, thus, the accuracy of the results depends on computing power and time. Within the framework of their DFT based stability calculations of the spinel and tetragonal hausmannite alloyed γ-Al_2O_3 structure with respect to the alloyed α-Al_2O_3 phase, Jiang et al. [27] proposed another pathway to obtain an adequate description of the γ-Al_2O_3 structure: Among the alloying candidates studied Si, Cr and Sc showed consistent stability trends while Ti and Y exhibited different stability predictions for these two configurations. While the Ti alloyed hausmannite configuration was reported to stabilize γ-Al_2O_3 with respect to Ti alloyed α-Al_2O_3 phase, the Ti alloyed spinel configuration exhibited a stabilization of the Ti alloyed α-Al_2O_3 phase. For Y the stability predictions were less conclusive with an energetic difference of - $1x10^{-1}$ meV/atom between the Y alloyed α-Al_2O_3 phase and spinel configuration and - 4.2 meV/atom between the Y alloyed α-Al_2O_3 phase and hausmannite configuration. The authors, thereby, proposed alloying with Ti and Y as key experiment to derive an experimentally suitable structure model for the γ-Al_2O_3 phase. However, as this proposal was based on the assumption that the Ti and Y are substituting Al cations in the γ-Al_2O_3 structure, experimental verification is restricted to a scenario where Ti or Y are in fact incorporated in the γ-Al_2O_3 structure and no chemical decomposition takes place. Thus, on the basis of the afore mentioned negligibly small energy differences obtained between the theoretically derived structure models for γ-Al_2O_3, the spinel, non-spinel and tetragonal hausmannite configuration may be considered as useful description of the γ-Al_2O_3 phase. As the synthesis conditions of γ-Al_2O_3, such as the employment of a substrate bias, may induce stress and strain which promotes peak shifting of the diffraction data, verification of the respective structure models by comparison of the simulated

diffraction pattern with experimentally derived diffraction data may cause inconsistency [40].

Furthermore, as mentioned earlier, the metastable nature of γ-Al_2O_3 which may lead to the simultaneous formation of additional Al_2O_3 polymorphs, such as the δ-/θ-phase at elevated temperatures, may interfere with the interpretation of γ-Al_2O_3 diffraction peaks. These reasons as well as the aforementioned complexities faced during experimental and computational analysis underline the challenges of studying the structure of the γ-Al_2O_3 phase. The DFT calculations performed within the scope of this thesis were done by using the traditional spinel-type structure of γ-Al_2O_3 with a 160 atom super cell reported by Paglia et al. [40].

For the remaining metastable Al_2O_3 phases, the structure of the δ-Al_2O_3 phase is reported as orthorhombic (space group $P2_12_12_1$) [29] but discrepancies exist regarding the presence of this phase. Some authors [46] - [48] proposed no experimentally observed difference between the γ- and δ-Al_2O_3 phase, while other studies reported evidence for a γ- to δ-Al_2O_3 transition [49], [50]. The best defined structure among the metastable alumina phases is assigned to the θ-Al_2O_3 phase with a monoclinic symmetry (space group C2/m). Table 2 presents selected properties of the most relevant metastable alumina phases. The transition alumina γ-, δ-, θ-Al_2O_3 are widely used as catalyst in chemical processes because of their catalytic activity and high surface area [9] - [11]. Due to their metastable nature, these phases transform to α-Al_2O_3 at elevated temperatures which limits their application range. Hence, the key to thermal stability enhancement is the suppression of

the transformation of the metastable γ-Al_2O_3 into the thermodynamically stable α-Al_2O_3 phase.

Phase	Space group	Density ($g \cdot cm^{-3}$)	Young's Modulus (GPa)
γ-Al_2O_3	$Fd\bar{3}m$	3.65 - 3.67 [51], [29]	253 [52]
δ-Al_2O_3	$P2_12_12_1$	3.6 - 3.65 [29]	-
θ-Al_2O_3	C2/m	3.6 - 3.65 [29]	-

Table 2: Selected properties of the most relevant metastable alumina phases.

2.2 Growth of alumina thin films

Although the thermodynamically stable α-Al_2O_3 phase is often used for applications at high thermal and mechanical load, the required deposition temperature in excess of 1000°C [13] limits the use of available substrate materials. Several pathways for the low temperature deposition of the α-Al_2O_3 phase were investigated in the past (Fig. 2). Jin et al. [53] demonstrated growth of α-Al_2O_3 at 400°C and a low deposition rate of 1 nm/min by non-reactive rf magnetron sputtering from an Al_2O_3 target using a chromia (Cr_2O_3) template. Wallin et al. [54] reported the deposition of α-Al_2O_3 at a temperature of 650°C on Mo substrates with floating potential and with applied bias of up to -100 V by using reactive high-power pulsed magnetron sputtering (HPPMS). Moreover, Yamada-Takamura et al. [55] deposited α-Al_2O_3 films at temperatures lower than 500 °C using filtered cathodic arc technique and a negative substrate bias voltage up to - 300 V. Recently, Sarakinos et al. [17] reported the synthesis of α-Al_2O_3 at 720°C and a bipolar pulsed substrate bias potential of – 40 V by using a monoenergetic, single charged Al^+ beam with defined ion

energy of 1 eV generated in a filtered cathodic arc system. The above mentioned studies emphasize the relevance of high energetic species for the synthesis of α-Al_2O_3 at low temperatures. Furthermore, molecular dynamic (MD) simulations performed by Music et al. [16] indicated that surface and bulk diffusion related mechanisms may be important during low-temperature growth of alumina films. The authors reported that Al bombardment induced fast diffusion along γ-Al_2O_3 (001) which gives rise to preferential α-Al_2O_3 (0001) growth [16]. The incoming Al ions with a kinetic energy of 40 eV caused preferential irradiation damages of γ-Al_2O_3 and, therefore, larger mobility in γ-Al_2O_3 compared to α-Al_2O_3.

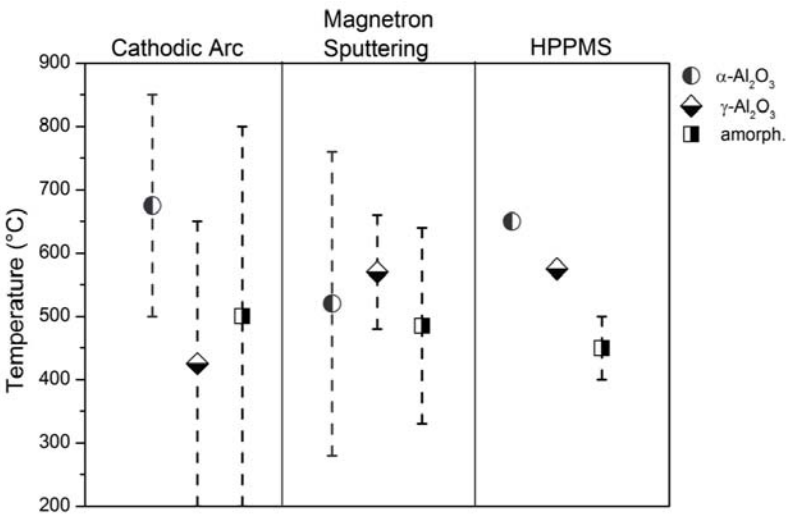

Fig. 2: Growth temperatures of amorphous, γ- and α- Al_2O_3 for different PVD methods [17], [18], [54], [57] – [59].

The growth of the metastable alumina phases, such as γ-, δ-, θ-Al_2O_3 are observed at lower synthesis temperatures. For chemical vapour deposition (CVD) the phase formation of γ-Al_2O_3 is obtained at 800°C [56]. For physical vapour deposition (PVD) Musil et al. [57] reported the formation of γ-Al_2O_3 at 500°C for magnetron sputtered alumina thin films. The transition from γ- to α-Al_2O_3 at 1050°C was thereby observed with an additional formation of θ-Al_2O_3. The transition from γ- to α-Al_2O_3 at 1050°C was thereby observed with an additional formation of θ-Al_2O_3. Furthermore, Edlymayr et al. [50] observed the formation of the intermediate δ-Al_2O_3 phase at 900°C in addition to γ-Al_2O_3. The intermediate γ-/δ-Al_2O_3 phases then transformed to α-Al_2O_3 at 1100°C. The indirect γ- to α-phase transformation via the formation of a metastable δ-, θ-phase is common in literature [29] while observations of a direct γ- to α-phase transformation are also possible [50], [60]. According to Eklund et al. [60] the different phase transformation paths may depend on the initial fraction of the γ-Al_2O_3 phase in the as-deposited films. While a low initial γ-phase fraction results in an indirect phase transformation, as-deposited thin films with a high crystalline γ-Al_2O_3 fraction give rise to a direct transformation [60]. Based on the different synthesis pathways reported for the individual Al_2O_3 phases it is evident, that aside from the synthesis temperature, ion energy and substrate material are a major factor influencing the phase formation of Al_2O_3 thin films. By using ion irradiation during the growth of Al_2O_3 thin films control of microstructure and phase evolution is obtained, which allows tailoring of thin films properties at kinetically limited low-temperature synthesis [17], [50], [55]. Furthermore, the application of templates, such as Cr_2O_3 [54], which resulted in local epitaxial growth of α-Al_2O_3 at 400°C, underline the importance of substrate material and structural templates for the low temperature synthesis of α-Al_2O_3. In turn, the use of

substrate materials such as Si, which has been reported to restrain the α-Al_2O_3 phase formation by stabilizing the metastable γ-Al_2O_3 phases [27], may aggravate the low temperature synthesis of α-Al_2O_3.

2.3 The effect of alloying elements on the stability of metastable alumina phases

Enhancing the thermal stability of the metastable alumina phases may enable the application of the metastable phase at high temperature processes. An effective strategy is alloying which may enhance the thermal stability of the metastable phases and, thereby, restrain the α-Al_2O_3 phase formation. The following two subchapters summarize the experimental and theoretical results reported in literature regarding the effect of alloying elements on the thermal stability of metastable alumina phases. With regard to the topic of this thesis, the major focus of this review is set on the results reported by using Si and Y as alloying elements.

2.3.1 Experimental

The effect of alloying elements, e.g. Er [23], La [24], Sr [25] and Y [23] and Si [26] on the thermal stability of alumina polymorphs was experimentally investigated in the past. However, the underlying mechanisms driving the observed retardation of phase transitions, with focus on Si and Y as alloying elements, are not fully understood.

With focus on Y as alloying element, experimental studies indicate precipitation of Y as $Y_3Al_5O_{12}$ (yttrium aluminum garnet, YAG) phase or other yttrium aluminate phases at the grain boundaries of the alumina matrix and only a low solubility of < 10 ppm in the α-Al_2O_3

structure [61], [62]. Furthermore, contradictive results were reported for the effect of Y on the γ- to α-transition. Some authors reported a delay of the γ- to α-Al_2O_3 phase transformation upon Y alloying [62], [63], whereas other studies provided opposite conclusions, i.e. an acceleration of the α-Al_2O_3 phase formation [64], [65]. It has been proposed that Y may affect the properties of metastable alumina phases and their transformation into α-Al_2O_3 by microstructural effects such as by providing availability of additional sites for heterogeneous nucleation of the oxide [66] as well as hampering the grain growth of metastable alumina phases [66]. A possible explanation for these controversies is proposed by Jedliński et al. [66] based on the effect of additives on the phase evolution of alumina-forming alloys. The authors surmised that a small Y content accelerates the transformation while a relatively high Y additive concentration to alumina-forming alloys may restrain the transformation. However, the authors did not report concentration limits which define the accelerating/retarding transformation effect of Y.

For Si alloying, Iler et al. [67] reported the thermal stabilization of γ-Al_2O_3 by 150°C by addition of silicic acid to fibrillar colloidal AlO(OH) (boehmite). The authors postulated the formation of a glassy and viscous phase upon the reaction of silica with alumina, in which silica wets the alumina surface and thereby restrains the migration of alumina. However, no experimental evidence was given in support of this notion. Gani and McPherson [68] studied the structure of Al_2O_3-SiO_2 sub-micron powders which were prepared by oxidation of aluminium-silicon halides in an oxygen-argon high frequency plasma flame. The authors reported that the addition of SiO_2 restrained the formation of α-Al_2O_3 from 1230°C to temperatures ≥ 1500°C. The restrained transformation of the metastable γ-/δ- and θ-Al_2O_3 phases to α-Al_2O_3 was suggested to be due to an increase of the activation energy of the

γ-/δ- and θ-Al_2O_3 to α-Al_2O_3 transformation process. The authors suggested that the incorporation of Si ions at tetrahedral sites of the initial γ-Al_2O_3 structure may increase the activation energy of the α-Al_2O_3 phase formation as high energy is required to break Si-O bonds in the distorted face centered cubic packing of oxygen ions of γ-Al_2O_3 phase and rearrange oxygen ions to the close packed hexagonal packing of the α-Al_2O_3 phase. Mekasuwandumrong et al. [26] investigated the thermal stability of χ-alumina solutions synthesized by solvothermal methods and reported a retardation of 100°C of the α-Al_2O_3 formation. They inferred a homogeneous incorporation of silicon atoms in the alumina matrix based on the crystallization of mullite which according to the authors requires atomic-scale mixing of alumina and silica. The increased thermal stability of χ–alumina was argued to be due to the reduction of hydroxyls in the Si alloyed alumina. Yoldas et al. [69] investigated the effect of silicon addition on monolithic active alumina prepared by sol-gel method and reported a retardation of the α-Al_2O_3 formation from 1200°C to 1380°C upon 6% alloying. The authors speculate that silicon occupies certain sites in the alumina structure without specifying the substitutional sites. These substitutions were assumed to cause disturbance in the lattice and restrain phase transition by increasing the structural stability of the alumina structure.

On the basis of the research discussed above it can be learned that the addition of Si to alumina appears to retard the alumina transformation sequences and stabilize the metastable γ-/δ-/θ-phases. However, different mechanisms leading to this retardation effect are proposed in the literature. Iler et al. [67] suggest that the formation of a glassy silica phase decreases mobility as schematically depicted in Fig. 3a. Other studies [26], [68], [70] suggest on the other hand that the enhanced stability of metastable phases is

due to incorporation of Si into the alumina lattice, usually referred to as Si incorporated intermediate Al_2O_3 or Al-Si spinel phase, as schematically shown in Fig. 3b. This Si incorporation notion has been a point of controversy in many studies [70] - [76]. The Al-Si spinel phase exhibits poorly defined X-ray diffraction peaks similar to those of γ-Al_2O_3. To clearly distinguish the diffraction peaks originating from γ-Al_2O_3 and from a Al-Si spinel phase based on XRD data is hence challenging.

Chakraborty et al. [75], [76] suggested based on TEM analysis of leached samples that the spinel type transition phase, which is observed during the kaolinite-mullite transition sequence, reveals an Al-Si spinel with compositions similar to mullite (Al_2O_3/SiO_2 ratio of 3/2). Similar suggestion was made by Okada et al. [73] by using analytical TEM. In contrast to these findings Brown et al. [77] deduced by Si nuclear magnetic resonance (NMR) spectroscopy pure γ-Al_2O_3 as intermediate phase of the kaolinite-mullite reaction sequence. Similar results were reported by Hoffman et al. [74] and Wei et al. [78] by using TEM analysis and Si NMR spectroscopy. The authors concluded that the spinel phase was Si-free γ-Al_2O_3 and no evidence for a Al-Si spinel was found.

Gerardin et al. [70] investigated the effect of mixing homogeneity of three stoichiometric sol-gel precursors prepared in three different ways on the phase formation sequence of mullite by NMR, X-ray diffraction and drop solution calorimetry. The results obtained by Gerardin et al. suggest that the degree of intermixing of alumina and silica in the amorphous state is determining the crystallization path and therefore the possibility and temperature of Al-Si spinel formation, silica segregation and mullitization.

The question whether Si is incorporated into PVD γ-Al_2O_3 grains (Fig. 3b) or is segregated at the grain boundaries (Fig. 3a and c) remains unanswered. From this review it is also evident that the underlying mechanisms responsible for the experimentally reported

enhanced thermal stability of the metastable alumina phases upon Si alloying are controversially debated for other synthesis pathways than PVD.

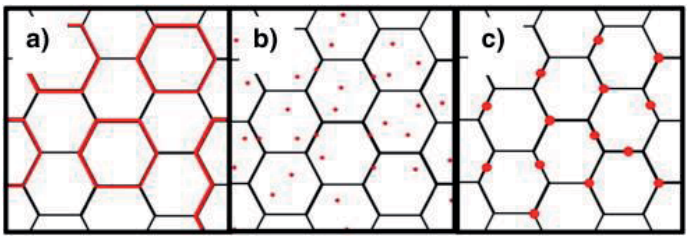

Fig. 3: Schematics of a) SiO_2 wetting of Al_2O_3 grains/grain boundaries, b) Si incorporation into the Al_2O_3 matrix and c) segregation of SiO_2 regions between Al_2O_3 grains. Hexagons indicate Al_2O_3 grains and red areas symbolize the presence of SiO_2.

2.3.2 Theoretical

All theoretical efforts in describing the phase stability of alumina polymorphs on the atomistic level assume that the alloying element is incorporated into the metastable alumina phases:

Comparative density functional theory (DFT) studies on θ- and α-Al_2O_3 by Wallin et al. [28] revealed that addition of Mo, W, Sc, Si, B, Cu, Cr and Co influence the stability of the θ-Al_2O_3 phase. It was reported that Cu stabilizes α-Al_2O_3 while the other additives shift the relative stability towards θ-Al_2O_3. Jiang et al. [27] investigated the effect of Si, Cr, Ti, Sc and Y additives on the relative stability of γ-Al_2O_3 with respect to α-Al_2O_3. By using ab initio calculations, the authors proposed that addition of Si with 2.5 at.-% at octahedral sites stabilizes the γ-Al_2O_3 with respect to α-Al_2O_3 while addition of Cr at the same concentration level and cation site stabilizes α-Al_2O_3. The contrary effect of Si and Cr on the relative stability was thereby explained based on the electron density distribution and bond

strength between additive cations and oxygen anions. While strong Si-O bonds stabilized γ-Al_2O_3, the presence of weaker Cr-O bonds shifted the relative stability towards α-Al_2O_3. Furthermore, Jiang et al. [27] performed a comparison between two additive alloyed γ-Al_2O_3 structure proposals based on cubic spinel and tetragonal hausmannite. However, the authors observed inconsistent stability predictions for the two γ-Al_2O_3 structures when Y additives were taken into account. For the spinel configuration the energetic difference between the Y alloyed γ-Al_2O_3 and α-Al_2O_3 phase was reported with - $1x10^{-1}$ meV/atom and for the hausmannite configuration with - 4.2 meV/atom. The experimental investigation of the γ- to α-transformation for Y alloyed γ-Al_2O_3 was thereby proposed as a key experiment in the context of describing the γ-Al_2O_3 structure.

Maglia et al. [79] performed atomistic simulations based on pair-wise interatomic potentials to study the energetics of trivalent cation incorporation with a concentration of 1.56 at.-% for additives such as Ga^{3+}, Fe^{3+}, Lu^{3+}, Y^{3+} in γ-Al_2O_3. The results suggested enhanced solubility of the trivalent cations in the γ-Al_2O_3 structure with respect to α-Al_2O_3, indicating phase separation and grain boundary segregation during the γ- to α-Al_2O_3 transformation. In addition, formation of trivalent cation and aluminum vacancy defect clusters located at first neighboring cation sites were proposed to restrain the γ- to α-Al_2O_3 transformation. The authors suggested that the formation of defect clusters may affect aluminum migration in the vicinity of the cation vacancies and, thereby, hinder the γ- to α-Al_2O_3 transition.

Although the majority of theoretical studies summarised in this section addressed fundamental questions regarding the impact of different additives on the relative stability of the metastable Al_2O_3 phases with respect to α-Al_2O_3, the small size of the supercells restricted the accuracy of the calculations and the additive concentrations used within these studies. Thus, to obtain accurate results with experimental relevance, larger

supercells with 160 and 80 atoms were used within the framework of this thesis, which allowed for calculations based on smaller concentrations of additives as well as more additive atoms in the same supercell, to study the interaction between the additives.

3. Methods of research

3.1 Theoretical methods

3.1.1 Ab initio calculations

Density functional theory (DFT) is a quantum mechanical formalism describing the electronic ground state properties of matter. The formalism is based on the Hohenberg-Kohn theorems [80] where the 1st theorem demonstrates that for non-degenerate ground states, the external potential $v_{ext}(r)$ is defined by the ground state electron density $n(r)$ and is, thereby, a functional of thereof. The 2nd theorem states the variation principle and demonstrates that the ground-state density is the minimum of the density functional. Thus, minimizing the energy of the system according to the electron density, the ground state energy can be achieved.

The DFT calculations within this thesis were performed by using the Vienna *ab initio* simulation package (VASP) and the generalized gradient approximation (GGA) with an energy cut-off of 500 eV [80] - [83]. The calculations were done by using the spinel-type structure of γ-Al_2O_3 with a 160 atom super cell reported by Paglia et al. [84]. This super cell consists of a 1x1x3 array of the primitive spinel cell of the space group $Fd\bar{3}m$ in which the oxygen anions form an fcc lattice and Al^{3+} ions occupy octahedral and tetrahedral coordinated sites. Brillouin-zone integrations were performed by using Monkhorst-Pack *k*-point meshes of 3x3x1. Calculations for pure γ-Al_2O_3 and Si-/Y-containing γ-Al_2O_3 were carried out. Substitutions were performed by either replacing octahedral or tetrahedral Al

sites in order to calculate the energy differences between these two possible positions in the super cell. The ad hoc substitutions were performed

- for Si addition by replacing 1, 2, 3, 4, 6 and 8 Al atoms resulting in 0.6, 1.3, 1.9, 2.5, 3.8 and 5 at.-% of Si, respectively.
- for Y addition by replacing 1, 2, 3, 4, 6, 8 and 12 Al atoms resulting in 0.6, 1.3, 1.9, 2.5, 3.8, 5, 6 and 7.5 at.-% of Y respectively.

To obtain the relative stability between Si-containing γ- and α-Al_2O_3, corresponding calculations on α-Al_2O_3 were also performed by using an 80 atom supercell (2x2x2 rhombohedral unit cell). Considering that the α-Al_2O_3 supercell contains 80 atoms only, additive concentrations of

- 1.3, 2.5 and 5 at.-% Si
- 1.3, 2.5, 5, 6.3 and 7.5 at.-% Y

were treated for the respective configuration. Each super cell was relaxed by performing force minimization at constant volume. Energy of solution, relative stability, structural properties, density of states as well as bond stiffness as a function of additive concentration were calculated. Furthermore, the total energies of α-SiO_2 (space group $P3_221$) and Y_2O_3 (space group $Ia\bar{3}$) were calculated by using a 9 atom supercell and a 40 atom supercell, respectively. To calculate the total energy of O_2, a 10x10x10 Å³ supercell was used to diminish the long-range interactions due to periodic boundary conditions.

To determine whether $(Al,M)_2O_3$, where M denotes the additive cation, decomposes spontaneously into Al_2O_3 and M_xO_y, the energy of solution E_{sol} was calculated from the

total energies *E* of the supercells as a function of the corresponding additive content *x*. In the case of the γ-configuration, two reactants were considered, namely α-Al_2O_3 and γ-Al_2O_3.

For Si addition in and employing γ-Al_2O_3 as reactant the energy of solution was defined as $E_{sol\,(\gamma,\gamma)}$ and calculated as

$$E_{\,sol\,(\gamma,\gamma)} = E_{\gamma(Al_{64-x}Si_xO_{96})} + \frac{x}{4}E_{O_2} - \frac{x}{3}E_{Si_3O_6} - \frac{64-x}{64}E_{\gamma(Al_{64}O_{96})}. \qquad \text{Eq. 1}$$

$E_{sol\ (\gamma,\alpha)}$ defined the energy of solution for Si addition in γ-Al_2O_3 employing α-Al_2O_3 as reactant and was calculated as

$$E_{sol\,(\gamma,\alpha)} = E_{\gamma(Al_{64-x}Si_xO_{96})} + \frac{x}{4}E_{O_2} - \frac{x}{3}E_{Si_3O_6} - \left[2\left(\frac{32-x/2}{32}\right)E_{\alpha(Al_{32}O_{48})}\right] \qquad \text{Eq. 2}$$

For Si addition in α-Al_2O_3 the energy of solution $E_{sol\,(\alpha,\alpha)}$ was calculated as

$$E_{sol\,(\alpha,\alpha)} = E_{\alpha(Al_{32-x}Si_xO_{48})} + \frac{x}{4}E_{O_2} - \frac{x}{3}E_{Si_3O_6} - \frac{32-x}{32}E_{\alpha(Al_{32}O_{48})}. \qquad \text{Eq. 3}$$

The energy of solution E_{sol} for Y addition in γ-Al_2O_3 was defined as $E_{sol,Y\,(\gamma,\gamma)}$ and calculated by the total energies E of the alloyed supercell as

$$E_{sol\ (\gamma,\gamma)} = E_{\gamma(Al_{64-x}Y_xO_{96})} - \frac{x}{16}E_{Y_{16}O_{24}} - \frac{64-x}{64}E_{\gamma(Al_{64}O_{96})}. \qquad \text{Eq. 4}$$

For Y addition in α-Al_2O_3 the energy of solution $E_{sol,Y\,(\alpha,\alpha)}$ was calculated as

$$E_{sol\,(\alpha,\alpha)} = E_{\alpha(Al_{32-x}Y_xO_{48})} - \frac{x}{16} E_{Y_{16}O_{24}} - \frac{32-x}{32} E_{\alpha(Al_{32}O_{48})}. \qquad \text{Eq. 5}$$

The energy of solution at 0 K obtained using Eq. 1 - 5 can be used to derive final temperature properties as for instance carried out by Hine et al. [83]. From the energy-volume data the equilibrium volume, the bond stiffness and the total energy of the system were obtained. For reference, calculations on pure alumina were carried out first. The results obtained for the lattice parameter of the α- and γ-phase are shown in Table 3. It can be seen that the calculated lattice parameters are in reasonable agreement with literature exhibiting a deviation of 0.5 – 1.4 % and ~ 0 - 1.3 % for α-Al_2O_3 and γ-Al_2O_3, respectively (see Table 3).

Phase	Space group	Lattice parameter (Å)		
		This work	Literature	
			Calculation	Experimental
α - Al_2O_3	$R\bar{3}c$	4.820	4.796 (GGA) [27]	4.762 [85]
			4.790 (LDA) [85]	
			4.751 (GGA) [86]	
γ - Al_2O_3	$Fd\bar{3}m$	7.996	7.990 (GGA) [86]	7.911 [42]
			7.960 (GGA) [27]	
			7.887 (LDA) [42]	

Table 3: Crystallographic data for α- and γ-Al_2O_3.

The fact that the calculated lattice parameters are slightly larger than the experimental values is a consequence of the usage of GGA functionals. While employing the local density approximation (LDA) leads to overbinding and, hence, shorter lattice parameters,

the semi local GGA gives rise to slightly longer lattice vectors, usually closer to the experimental values [82], [87].

Studies on the effect of Si/Y on the electronic structure of the γ- and α-phase were carried out by calculating the total and partial density of states (DOS). The bond stiffness was obtained from the linear fit of the Si/Y - O bond lengths (relative to the shortest Al-O bond of pure γ-Al_2O_3) in γ- and α-Al_2O_3 as a function of pressure. The linear coefficient of the linear fit for each phase defined the bond stiffness and was studied as a function of Si/Y concentration. Smaller linear coefficient values can be assigned to stiffer bonds.

3.2 Experimental methods

3.2.1 Filtered cathodic arc

Within the scope of this thesis the unalloyed and alloyed alumina thin films were synthesized by using an industrial filtered cathodic arc source (Nanofilm-Singapore), as shown in Fig. 4.

Modern practical cathodic arc systems consist of several fundamental components: a conductive cathode from which the plasma is emitted, an anode, which is basically an electron-collecting electrode, a trigger to initiate the discharge, a power supply, and a vacuum chamber. The cathodic arc technique describes a low-voltage, high-current glow discharge between two conductive electrodes in a vacuum. Unlike conventional discharges (for example sputtering) which require an ionized gas as a conductive medium,

the electrode material itself is used to sustain the discharge without the need for a background gas.

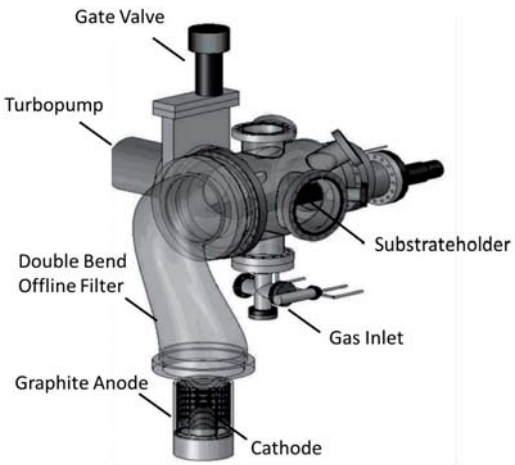

Fig. 4: Schematic overview of the industrial filtered cathodic arc setup used within this thesis.

The arc voltage is in the range of 10 - 30 V and varies according to the cathode material. The arc is initiated by a trigger which generates an energetic emitting area, the so called cathode spot on the surface of the cathode. The charge carriers in the cathode spot consist of 90 % electrons and 10 % ions. The spot size is determined to be in the range of 1–10 µm while current density values at the spots are estimated to be in the order of 10^6 – 10^8 A/m^2 [88]. The residence time of a cathode spot at a fixed location is determined to be in the range of 10 ns to 1 µs [89], [90]. New spots reignite at edges of previous spot locations which promotes the effect of so called light trajectories with a random-walk motion. The lower limit of arc current, called the chopping current, constricts the range below which the cathode spot will not persist. The upper limit of the arc current is

determined by cooling requirements of the cathode and the formation of anode spots [91]. The formation of cathode spots gives rise to a dense plasma which, driven by the high pressure gradient near the spot, drifts away from the surface with velocities in the range of 10^4 m/s [92]. Furthermore, the cathodic arc plasma provides the highest degree of ionization [93] which can be achieved by a PVD process. The high ionization level is advantageous in order to tailor the thin film quality by electrically biasing the substrate during deposition. Due to the high power density, the plasma is build up by multiply charged ions with energies in the range of 20 – 160 eV [88]. Charge state resolved ion energy distribution functions (IEDFs) of cathodic arc plasmas have been extensively studied [59], [94] in the past.

Cathodic arc systems can be operated either in continuous direct durrent (DC) or pulsed mode. The majority of cathodic arc systems are operated in the DC mode when high deposition rates are required. Pulsed cathodic arc systems are used in order to obtain a higher and reproducible plasma density than offered by DC cathodic arcs. By increasing the pulse frequency, the deposition rates can be tailored matching deposition rates obtained by DC cathodic arcs [93]. However, a crucial challenge of pulsed cathodic arc systems is the high concentration of hydrogen incorporated into the coating which may affect coating quality and phase formation [93].

Furthermore, another challenging aspect in the application of cathodic arcs for thin film deposition is the contamination of the thin film by droplets of the cathode material. These droplets are caused by the molten phase of the cathode spots which is partially dragged along by the plasma beam. Despite their small diameter of a few micrometers, these droplets are termed macroparticles due to their large size as compared to the ions in the

plasma [95] - [97]. As an effect of their velocity (up to 100 m/s) and despite their heavy mass, these macro particles may easily reach the substrate and degrade the quality of the films. For example, macroparticles on coatings could avoid their application to more demanding areas as precision optics and electronics where smooth and defect-free films are required. A number of approaches are suggested for the removal of such macroparticles, foremost the use of filtering. The basic characteristic of most macroparticle filters is to electro-magnetically guide the plasma by a curved magnetic field to the substrate, which is located beyond the line of-sight of the cathode [97] - [99]. Macroparticles may be slightly charged but due to their large mass their trajectories are not influenced by electric and magnetic fields. Consequently, macroparticles will move unaffected by electro-magnetic fields and are removed to a large extent by magnetic filtering.

3.2.1.1 Si alloyed alumina thin films

The unalloyed and Si alloyed alumina thin films were synthesized at constant arc current of 110 A, a filter coil current of 15 A and an anode coil current of 9 A. One Al cathode (99.5% purity) and two Al-Si cathodes with 2.5 and 10 at.-% of Si were used to deposit the reference Al_2O_3 film and the two silicon alloyed alumina thin films. The diameter of the cylindrical unalloyed and Si alloyed cathodes was 70 mm, respectively. All depositions were performed at 650°C substrate temperature in an Ar-O_2 ambient at a working pressure of 1 Pa and an oxygen partial pressure of 3.2 mTorr. Si(100) wafers were used as substrate materials for deposition of unalloyed and Si alloyed alumina thin films. The substrate was kept at stationary mode and on a floating potential of – 8 V for all

depositions. Furthermore, all depositions where performed by using a monoenergetic Al^+ plasma beam with an average ion energy of 1 eV, as described elsewhere [94].

3.2.1.2 Y alloyed alumina thin films

Unalloyed and Y alloyed alumina thin films were synthesized by using an industrial filtered cathodic arc source (Nanofilm-Singapore) at constant arc current of 110 A, a filter coil current of 15 A and an anode coil current of 9 A. One pure Al cathode (99.5% purity) and three Al-Y cathodes with 2.5, 5.0 and 10.0 at.-% Y, respectively, were used to deposit Al_2O_3 thin films with different Y concentrations. The depositions were carried out at in an Ar-O_2 ambient at a working pressure of 1Pa and a substrate temperature of 650°C. Two series of thin films were deposited at a floating - 8 V and - 130 V substrate bias potential. Pulsed DC substrate bias potential with a frequency of 100 kHz and a duty cycle of 90% was used. The substrates were deposited in stationary mode. Si(100) wafers were used as substrate material and cleaned with methanol in an ultrasonic bath prior to deposition. Furthermore, all depositions where performed by using a monoenergetic Al^+ plasma beam with an average ion energy of 1 eV, as described elsewhere [94].

3.2.2 Thin film characterization

Compositional analysis of the as-deposited thin films was performed by energy dispersive X-ray analysis with an EDAX Genesis 2000 analyser at an acceleration voltage of 6 kV. The oxygen to metal ratio was analysed to be stoichiometric with 1.5 for the unalloyed and alloyed samples.

To investigate the chemical state of the as-deposited unalloyed and alloyed alumina films, X-ray photoelectron spectroscopy (XPS) was employed by using a JAMP-9500 F system (JEOL) with a *Kα* Mg X-ray source (energy 1253 eV) and a hemispherical electron energy analyser with a pass energy of 20 eV. Binding energies were determined utilizing the C1s line from adventitious carbon with the energy of 284.5 eV as reference to correct for peak shifts. All spectra were corrected by subtracting a Shirley-type background [98]. Curve fitting was performed by using CASA XPS (V 2.3.15) software (CASAXPS Software Ltd. UK). The curve fitting parameters (FWHM and Gaussian/Lorentzian ratio of 70/30) were determined by taking the unalloyed sample as reference. By keeping the FWHM and Gaussian/Lorentzian peak shape constant for each core level, only fitting with two components appeared meaningful for the Si alloyed samples.

Post-annealing of the as-deposited films on Si(100) wafers was performed by using a furnace with a heating and cooling rate of 10°C/min (HTF-1700, Carbolite). Sequential annealing was performed for each sample at temperatures in the range of 800°C - 1300°C in ambient air. The samples were held for 1 hour at the respective annealing temperature. The phase formation of the as-deposited and post-annealed aluminum oxide films was investigated by X-ray diffraction (XRD) at a constant incident angle of 15° using a Bruker D8 with the general area detection diffraction system (GADDS) with Cu Kα radiation and a collimator of at 40 kV and 40 mA. Additional high resolution XRD of the Al_2O_3 thin films with 0 and 2 at.-% Si was performed by using a SIEMENS D5000 with Cu Kα radiation with a step size of 0.002° in Bragg-Brentano geometry. The phases were identified by comparing the recorded diffraction pattern with reference patterns given in the JCPDS cards for various Al_2O_3 polymorphs, aluminosilicates and yttrium aluminates. Moreover,

the crystallite size as function of annealing temperature was estimated by the high resolution XRD results using the Debye - Scherrer equation [100]

$$D = \frac{K\lambda}{\beta \cos \theta} \qquad \text{Eq. 6}$$

where D is the average crystallite size, K is constant equal to 0.94 here, λ is the wavelength of the X-ray radiation (Cu Kα, 0.15406 nm), β is the corrected line broadening after subtraction of equipment broadening, and θ is the diffraction angle. Transmission electron microscopy (TEM) sample preparation of the unalloyed and alloyed alumina thin films deposited on Si(100) wafers was performed by Focused Ion Beam using a FEI Strata FIB 205 workstation. The TEM investigation was carried out in a FEI Tecnai F20 transmission electron microscope operated at 200 kV. To characterize the samples, conventional transmission electron microscope techniques were applied. TEM bright field (TEM BF) images were recorded to illustrate the morphology of the layers and selected area diffraction (SAD) pattern were taken into account to analyze the film structure.

4. Results and Discussion

4.1 The effect of Si on the phase stability of Al_2O_3 polymorphs

4.1.1 Introduction

Although the theoretical studies on the effect of Si on the phase stability of Al_2O_3 phases summarised in section 2.3.2 addressed some major questions concerning the effects of additives on the relative stability of the metastable Al_2O_3 phases with respect to α-Al_2O_3, the small size of the supercells restricted the minimal additive concentrations. A larger supercell, however, would allow for higher accuracy of the calculation and smaller concentrations of additives. Furthermore, the reason for including more additive atoms in the same supercell is to allow for possible interactions between the additives and to study the effect of different additive concentrations on the stability of γ-Al_2O_3 with respect to α-Al_2O_3, which is of experimental relevance and cannot be accounted for in small supercells with periodic boundary conditions. Additive interactions can have a large effect on phase stability. For $Ti_{1-x}Al_xN$, it was shown that clustering into TiN and AlN rich regions increases the metastable solubility limit of Al in the NaCl structure from x = 0.64 to 0.74 [101]. Recently, clustering of TiN and AlN in TiAlN has also been observed experimentally [102]. In the following section, we therefore use large supercells with 160 atoms for the γ-phase and 80 atoms for the α-phase which allow for 0–5 at.% Al substitution. Furthermore, the influence of crystal site occupation by Si on the relative stability of γ-Al_2O_3 with respect to α-Al_2O_3 is investigated by replacing octahedral and tetrahedral Al sites in the γ-Al_2O_3 supercell. The choice of the additive is motivated by the larger valency of the additive

cation to account for possible effects of increasing electron density on the bonding behavior of the atoms and thereby on the phase stability of γ- and α-Al_2O_3. Therefore, Si is chosen with a higher valency of four compared to Al which contains three valence electrons. It is shown that for $(Al,Si)_2O_3$, decomposition into α-Al_2O_3 and SiO_2 is energetically favored. The additive-element-induced changes in stability of the metastable solid solution are analyzed with respect to concomitant changes in electronic structure. To validate the obtained DFT results, the effect of different Si concentration on the thermal stability of silicon alloyed alumina thin films deposited by filtered cathodic arc is investigated systematically. The aim of this work is to identify the underlying mechanism responsible for the enhanced thermal stability of silicon alloyed alumina. It is shown that Si additions expand the stability window of metastable γ-/δ- and θ-Al_2O_3 phases and restrain the α-Al_2O_3 phase formation. Based on our phase formation and bonding data we suggest that the presence of intergranular SiO_2 impeding mobility is responsible for the Si addition induced changes in stability. The random distribution of Si in the alumina lattice appears to be in conflict with XPS data.

4.1.2 Ab initio study on the effect of Si on the phase stability of γ- and α-Al_2O_3

4.1.2.1 Effect of Si additives on the phase stability

To evaluate the phase stability of $(Al,Si)_2O_3$, the energy of solution was calculated using Eq. 1 - 3, respectively. For the γ-configuration, two reactants, namely α-Al_2O_3 and γ-Al_2O_3, were considered. Subsequent calculations investigating the effect of substitution site on the

stability were performed for γ-$(Al,Si)_2O_3$. To probe the effect of charge balance on the energy of formation while adding Si to γ-Al_2O_3, the extra charge of Si at a concentration of 1.9 and 3.8 at.-% was balanced with one and two Al vacancies, respectively.

Fig. 5 displays the energy of solution $E_{sol\ (\gamma,\gamma)}$ and $E_{sol\ (\alpha,\alpha)}$ for addition of Si in α-Al_2O_3 and γ-Al_2O_3. For the energy of solution $E_{sol\ (\gamma,\gamma)}$ γ-Al_2O_3 was assumed as reactant. The calculated data are fitted with a second order polynomial function. As shown in Fig. 5, the energies of solution are positive for all substitution sites in the γ- and α-phase. This indicates decreased chemical stability with increasing Si concentration for the γ- and α-phases which implies that decomposition is energetically favoured with the chemical driving force E_{sol}. The effect is stronger for the α-phase as compared to the γ-phase which is expected, since the less dense γ-phase may more easily accommodate the lattice distortion induced by the Si than the dense α-phase.

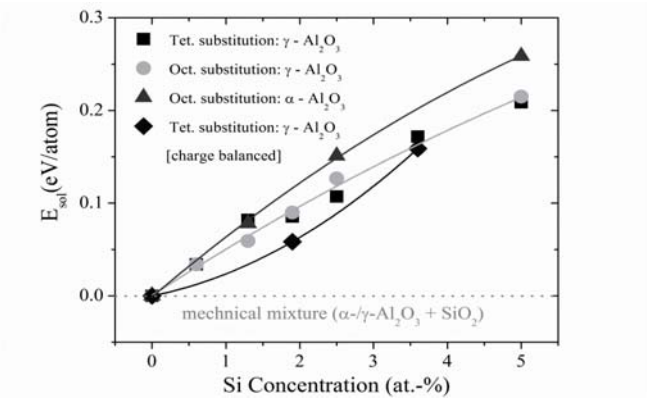

Fig. 5: $E_{sol\ (\gamma,\gamma)}$ for tetrahedral and octahedral substitution by Si in γ-Al_2O_3 and $E_{sol\ (\alpha,\alpha)}$ for octahedral substitution in α-Al_2O_3. The mechanical mixture of γ-/α-Al_2O_3 and SiO_2 is represented by the dotted line.

Due to the lower energy of the mechanical mixture for all compositions studied and the lower energy of formation of α-Al_2O_3 over γ-Al_2O_3, it can be concluded that the resulting phases of an equilibrium process of $(Al,Si)_2O_3$ is a mechanical mixture of γ-/α-(Al_2O_3) and SiO_2 or another compound not studied here. Therefore, γ-$(Al,Si)_2O_3$ is a metastable solution.

It is well known that metastable phases such as cubic $Ti_{1-x}Al_xN$ and $Cr_{1-x}Al_xN$ are readily formed during non-equilibrium growth using PVD even though cubic TiN (CrN) and hexagonal AlN represent the thermodynamically stable phases in these systems [103], [104]. The driving forces for decomposition of cubic $Ti_{0.5}Al_{0.5}N$ and $Cr_{0.5}Al_{0.5}N$ are in the range of 50 - 150 meV/atom, which are comparable to the energy differences obtained for 0.6 – 3.8 at.-% Si in this study [103], [104]. The reason for formation of a single cubic phase in vapor phase condensation is limited surface diffusion (also referred to as ad-atom mobility). Kinetically limited growth is caused by a low deposition temperature and/or low kinetic energy of the deposited flux. For $Ti_{0.5}Al_{0.5}N$ it was shown that decomposition into the stable compounds occurs at deposition temperatures around 560°C while a single cubic phase is observed at lower temperature [105]. Based on the data discussed above the formation of metastable phases can be expected for $(Al,Si)_2O_3$ during kinetically limited vapor deposition. No significant difference is obtained for Si located at tetrahedral or octahedral sites in the γ-phase. Furthermore, the difference in $E_{sol\ (\gamma,\gamma)}$ between the charge unbalanced and balanced state for tetrahedral coordination of Si in the γ-phase decreases from 27 meV/atom for 1.9 at.-% Si to 13 meV/atom for 3.8 at.-% Si. Hence, the general trend observed in $E_{sol\ (\gamma,\gamma)}$ for Si additions is not an artifact introduced by lack of charge balancing.

To study the effect of additive interactions on the $E_{sol\ (\gamma,\gamma)}$ of the γ-phase, further calculations were performed for Si concentration of 1.3 at-%. Therefore, the additive cations were either placed at tetrahedral positions near or far from each other in the host lattice. The calculations resulted in an energetic difference of 1 meV/atom between the two possible configurations, which suggests only a marginal effect of the Si interaction on $E_{sol\ (\gamma,\gamma)}$. As pointed out above, the energy of solution $E_{sol\ (\gamma,\alpha)}$ was also calculated for γ-$(Al,Si)_2O_3$ with respect to α-Al_2O_3 in contrast to Fig.5, where γ-Al_2O_3 was used as reference. Fig. 6 displays $E_{sol\ (\gamma,\alpha)}$ in comparison to $E_{sol\ (\alpha,\alpha)}$, which has been already used in Fig. 5. The calculated data are fitted with a second order polynomial function to estimate the stability regions for the γ- and α-solution phases. We do not propose any physical model for the observed dependence, but in order to describe the trend of the ab initio results, which exhibit scattering of data points, we use a second order polynomial fit.

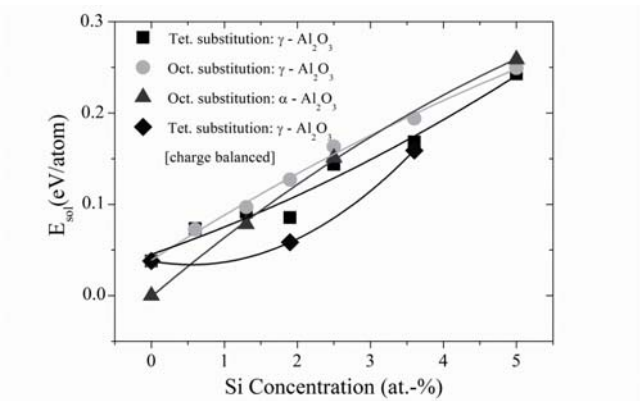

Fig. 6: $E_{sol\ (\gamma,\alpha)}$ for tetrahedral and octahedral substitution by Si in γ-Al_2O_3 and $E_{sol\ (\alpha,\alpha)}$ for octahedral substitution in α-Al_2O_3.

As shown in Fig. 6, Si stabilizes the γ-phase compared to the α-phase at a concentration of > 1.5 at.-% for tetrahedral substitution and at > 3 at.-% Si for octahedral substitution with respect to the Si alloyed α-phase. Upon charge balancing the tetrahedral coordination of Si in the γ-solution is stabilized compared to the α-solution for Si additions > 0.5 at.-%. Nevertheless, the general trends are preserved. This indicates that γ-$(Al,Si)_2O_3$ is expected to form during kinetically limited synthesis for Si contents larger 0.5 at.-%. The phase stability data discussed above may be understood based on the electronic structure: DOS and bond stiffness.

4.1.3 Effect of Si additives on the electronic structure

4.1.3.1 Density of states

We start our analysis with the effect of Si additives on the electronic structure, the DOS of γ- and α-Al_2O_3 are compared in Fig. 7a and b, respectively. The valence band of the pure γ- and α-Al_2O_3 consists of two subbands separated by a gap. The lower valence band is not shown here but it is mainly formed by oxygen 2*s* orbitals as well as of aluminum 3*s* and 3*p* orbitals. The upper valence band (the energy in the range -10 - 0 eV) is mainly formed by oxygen 2*p* and aluminum 3*s* and 3*p* orbitals. The estimated band gaps of the γ- and the α-phase are 4 and 6 eV, respectively, and are in good agreement with other calculations [106], [107] but are lower than the experimental values reported to be 7.0 and 8.8 eV [108], [109]. This discrepancy is evidently associated with the fact that DFT systematically underestimates the band gap width in solids [110]. For instance, this can be

improved by using the Hubbard approach or the perturbation theory, but this is outside of the scope of this work.

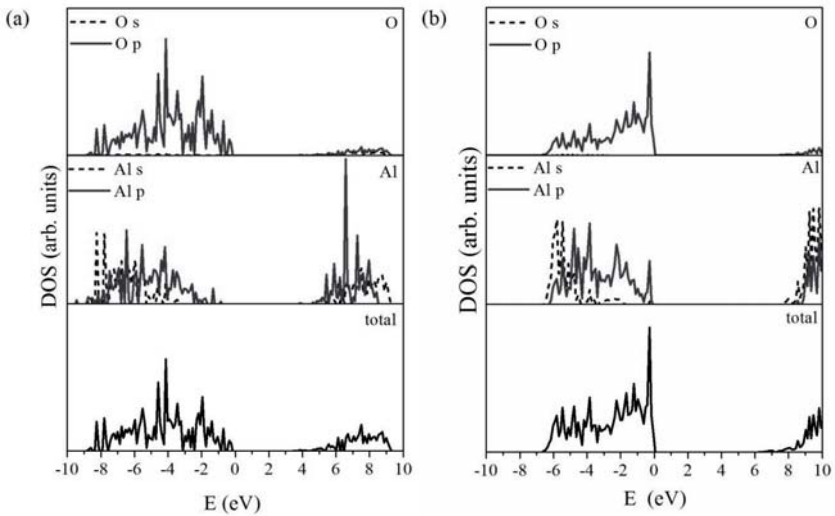

Fig. 7: Total and partial density of states of a) γ-Al_2O_3 and b) α-Al_2O_3. The Fermi level is set to 0 eV.

For addition of 5 at.-% Si (Fig. 8a and b), the replacement of Al by Si in the γ- and α-phase introduces additional states in the band gap. To establish if these defect states are only attributed to the extra valence electron of Si in comparison to Al, DOS of the charge unbalanced and balanced state at 3.8 at.-% Si were also analyzed (not shown here). Regardless of charge balance, both DOS show additional states in the band gap which underlines the low stability of the herein investigated Al_2O_3 phases with Si addition.

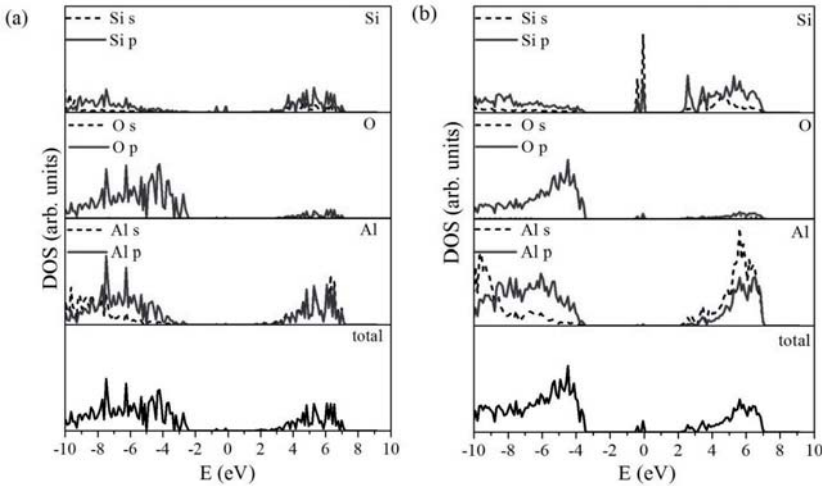

Fig. 8: Total and partial density of states of a) γ-Al_2O_3 with 5 at.-% Si at tetrahedral sites and b) α-Al_2O_3 with 5 at.-% Si at octahedral sites. The Fermi level is set to 0 eV.

4.1.3.2 Bond stiffness

To further investigate the effect of Si addition the stiffness of Si-O bonds is analyzed as function of Si concentration. The bond stiffness was obtained from the linear fit of the Si-O bond lengths (relative to the shortest Al-O bond of pure γ-Al_2O_3) in γ- and α-Al_2O_3 as a function of pressure. The linear coefficient of the linear fit for each phase defined the bond stiffness and was studied as a function of Si concentration. Smaller and negative linear coefficient values can be assigned to stiffer bonds. As shown in Fig. 9, the increase of Si concentration from 1.3 to 5 at.-% has no significant effect on the bond stiffness of the Si-O bonds in the γ-phase with tetrahedral coordination of Si. For octahedral coordination of Si in the γ-phase, a marginal decrease of bond stiffness is observed with increasing Si

concentration (increase of linear coefficient from -0.019 to 0.012 pm/GPa). When Si is added to the α–phase, the bond stiffness is only marginally affected for 1.3 at.-% Si and 2.5 at.-% Si, respectively (increase of linear coefficient from -0.03 to 0.018 pm/GPa). At 5 at.-% Si concentration, however, the octahedral coordinated Si-O bonds of the α-phase exhibit a sudden decrease of bond stiffness (increase of linear coefficient to 0.378 pm/GPa).

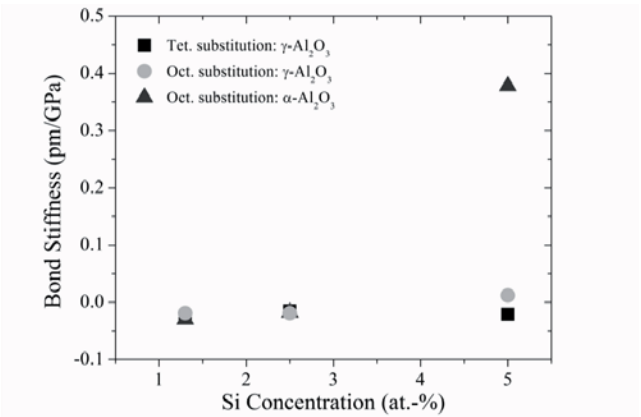

Fig. 9: Bond stiffness of Si - O bonds for tetrahedral, octahedral substitution by Si in γ-Al_2O_3 and octahedral substitution by Si in α-Al_2O_3 as a function of Si concentration.

Furthermore, at 5 at.-% Si, a partial Si-O bond breaking is observed when Si is located at octahedral substitution sites in the γ- and α-phase (not shown here). However, this effect is more pronounced for the α-phase as indicated in Fig. 9, where the increase of Si concentration leads to drastic decrease of bond stiffness. As Si is placed in an octahedral position, the octahedron is disrupted and less Si–O bonds are present. The observed distortion of the octahedron is consistent with *ab initio* results obtained by Wallin et al. [28]

where atoms smaller than Al, such as Si and B, placed at octahedral positions exhibited bond breaking with only four of the six oxygen atoms present around the additive atom. The lower bond stiffness of the α-phase compared to the γ-phase with increasing Si concentration is consistent with the observed stability regions of the α- and γ-solutions depicted in Fig. 6. Hence, based on the changes in bond stiffness and electronic structure induced by Si addition it is evident that the additive concentration as well as the occupation site significantly determines the stability regions of γ- and α-Al_2O_3. The calculations presented here describe an alloy composition range. This approach enables the identification of stability regions and is thus advantageous from a material design perspective compared to stability studies based on single concentration calculations.

4.1.4 The effect of Si additives on the phase formation of Al_2O_3 thin films deposited by filtered cathodic arc

4.1.4.1 Effect on the phase formation

To investigate the phase formation sequence of the unalloyed and Si-alloyed alumina thin films, X-ray diffraction was performed before and after annealing to temperatures in the range from 900°C to 1300°C. Fig. 10 displays the X–ray diffractograms of the unalloyed Al_2O_3 thin film in the as-deposited state and after post-annealing. To allow for a better distinction between the metastable γ-, δ- and θ-Al_2O_3 phases, additional high resolution XRD diffractograms of the 2θ range from 42 to 50° are shown as a function of the annealing temperature in the range of 650 – 1100°C in Fig. 11. The as-deposited thin film exhibits diffraction signals characteristic for γ-Al_2O_3. No evidence for the formation of other

phases can be seen, and no evidence for phase transformations in the temperature range from 650 to 900°C can be observed in Fig. 10 and 11.

In Fig. 11 it can be seen that at 1000°C the shoulders around the (400) peak (2θ = 45.86°) of the γ-phase indicate the presence of metastable δ- and θ-Al_2O_3 (space group C2/m) traces in addition to γ-Al_2O_3. A drastic phase change occurs between 1000°C and 1100°C where α-Al_2O_3 is evolving into the dominating phase. At 1200°C and 1300°C (Fig. 11) only the α-Al_2O_3 is present.

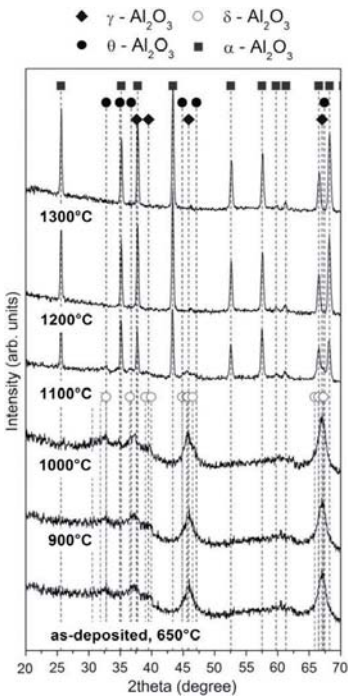

Fig. 10: X–ray diffractograms of unalloyed Al_2O_3 films after annealing at different temperatures for 1 hour in air.

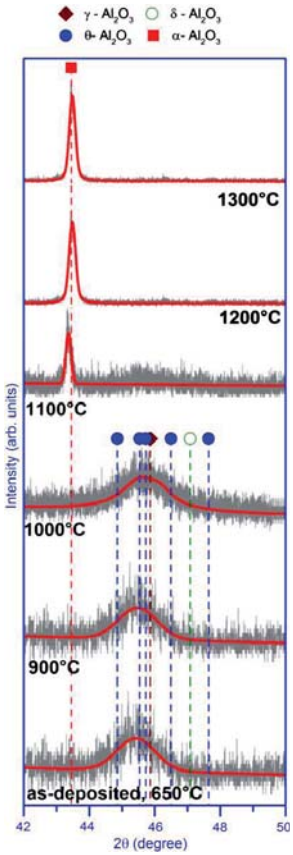

Fig. 11: High resolution diffractograms of the 2θ range 42 – 50° of the unalloyed Al_2O_3 film annealed in air.

This indirect γ- to α-phase transformation via the metastable δ-, θ-phase is consistent with literature [29], [60] while observations of a direct γ- to α-phase transformation are also reported [29], [111]. The phase formation sequence of the unalloyed Al_2O_3 film is γ-Al_2O_3 $\xrightarrow{650-1000°C}$ γ-Al_2O_3 + traces of δ- and θ-Al_2O_3 $\xrightarrow{1100-1300°C}$ α-Al_2O_3.

The film with 0.7 at.-% Si shows a different phase formation sequence compared to the unalloyed Al_2O_3 film (see Fig. 12 and 13). The as-deposited silicon alloyed alumina thin film is X-ray amorphous with traces of γ-Al_2O_3. The phase formation sequence is X-ray amorphous + traces of γ-Al_2O_3 $\xrightarrow{650-900°C}$ γ-Al_2O_3 $\xrightarrow{1000-1100°C}$ traces of γ-Al_2O_3 + δ- and θ-Al_2O_3 $\xrightarrow{1100-1200°C}$ δ- and θ-Al_2O_3 $\xrightarrow{1200-1300°C}$ Mullite + α-Al_2O_3 + traces of δ- and θ-Al_2O_3.

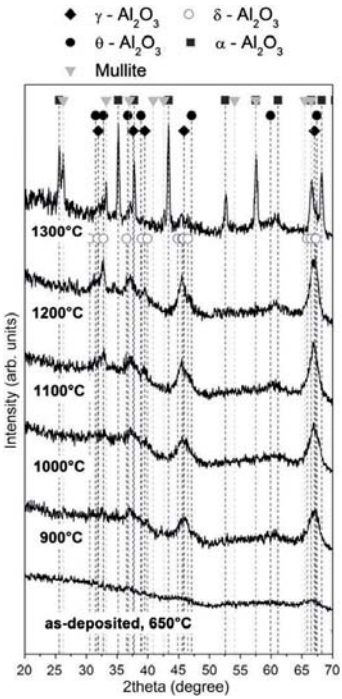

Fig. 12: X – ray diffractograms of the with 0.7 at.-% Si alloyed alumina thin film after annealing at different temperatures for 1 hour in air.

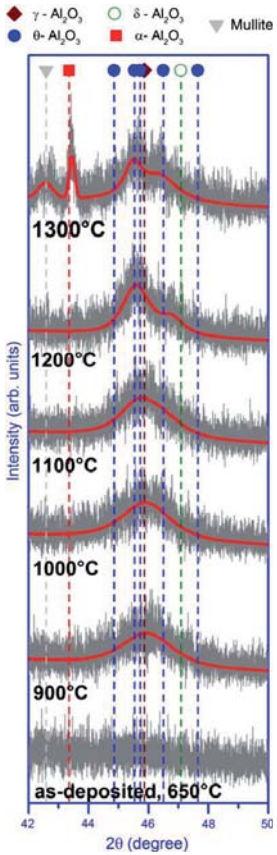

Fig. 13: High resolution diffractograms of the 2θ range 42 – 50° of the with 0.7 at.-% Si alloyed alumina thin film after annealing in air.

After annealing to 900°C, formation of γ-Al_2O_3 is observed (Fig. 13). At 1100°C, the metastable δ- and θ-phase are detected in addition to γ-Al_2O_3, which indicates a restrained δ- and θ-phase formation by 100°C compared to the unalloyed Al_2O_3 thin film (Fig. 13). At 1200°C the intensity of the δ- and θ-phase peaks is increasing. In contrast to the unalloyed

Al_2O_3 film, where the α-phase formation is already observed at 1100°C, the addition of 0.7 at.-% Si stabilizes the δ- and θ-phase to temperatures ≥ 1200°C and restrains the formation of the α-phase to temperatures between 1200°C and 1300°C (Fig. 13).

Moreover, there is evidence for the presence of mullite (space group Pbam) [112] in addition to α-Al_2O_3 at ≥ 1300°*:* Mullite diffraction signals are shown in the high resolution XRD of the 2θ range from 25 to 27° (Fig. 14). At 1300°C peak splitting of the (120) and (210) peak indicates the formation of orthorhombic mullite [112].

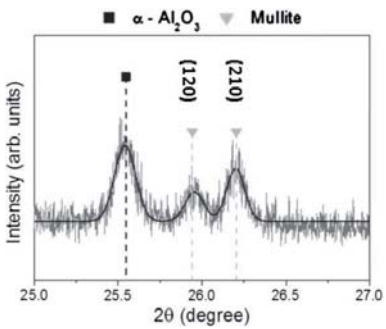

Fig. 14: High resolution X–ray diffractogram (2θ range of 25 – 27°) of the with 0.7 at.-% Si alloyed alumina thin film annealed at 1300°C in air.

The XRD diffractogram of the with 2 at.-% Si alloyed alumina thin film is X-ray amorphous in the as-deposited state and appears similar to the film containing 0.7 at.-% Si (see Fig. 15). For this sample also additional high resolution XRD was performed in the annealing temperature range of 650 - 1300°C (Fig. 16). The stepwise annealing of the alloyed alumina film to 1300°C reveals the following transition sequence: X-ray amorphous Al_2O_3 $\xrightarrow{650-900°C}$ γ-Al_2O_3 $\xrightarrow{1000-1100°C}$ traces of γ-Al_2O_3 + δ- and θ-Al_2O_3 $\xrightarrow{1100-1200°C}$ δ- and θ-Al_2O_3

$\xrightarrow{1200-1300°C}$ Mullite + δ- and θ-Al_2O_3 + traces of α-Al_2O_3 (Fig. 15 and 16). Furthermore, the intensity of the δ- and θ-Al_2O_3 peaks is increasing in the temperature range of 1100°C to 1200°C as it can be seen in Fig. 16. As the diffracted intensity of δ- and θ-Al_2O_3 is increasing the γ-Al_2O_3 intensity is decreasing, indicating a transition from γ- to δ- and θ-Al_2O_3 at > 1100°C.

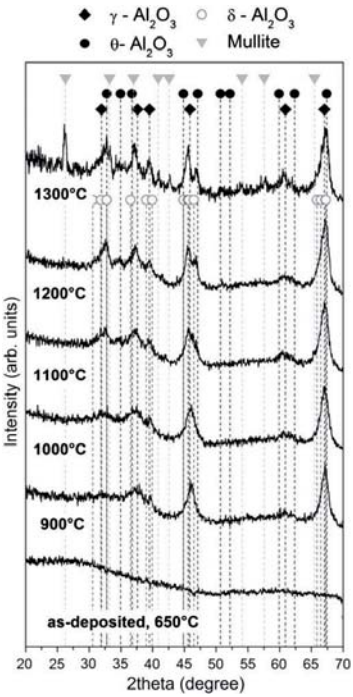

Fig. 15: X–ray diffractograms of the 2 at.-% Si alloyed alumina thin film after annealing at different temperatures for 1 hour in air.

The restrained δ- and θ-Al_2O_3 formation is similar to the transition sequence observed for the 0.7 at.-% Si alloyed alumina thin film. At temperatures ≥ 1300°C, the formation of mullite is observed in addition to the metastable δ- and θ-Al_2O_3 phases and some traces of α-Al_2O_3 (Fig. 15 and 16).

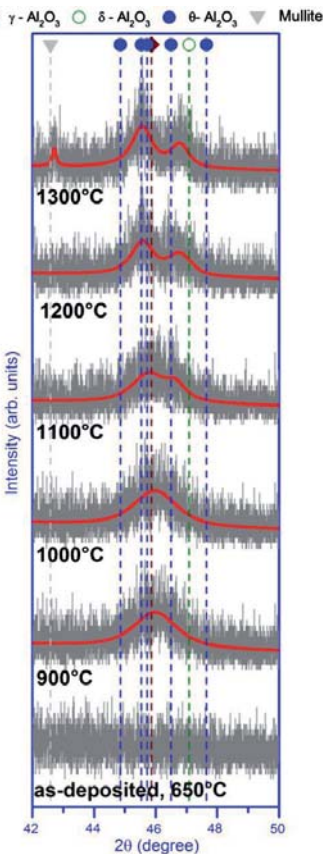

Fig. 16: High resolution diffractograms of the 2θ range 42 – 50° of the 2 at.-% Si alloyed alumina thin film after annealing in air.

Additional high resolution XRD of the 2θ range from 25 to 27° (Fig. 17) displays, consistent with the 0.7 at.-% sample, the peak splitting of the (120) and (210) peak which indicates the presence of orthorhombic mullite [112].

In the same figure, evidence for the formation of α-Al_2O_3 traces at 1300°C can be seen. In the 0.7 at.-% sample the diffracted intensity of α-Al_2O_3 was larger and the mullite intensity smaller than in the 2 at.-% sample. Generally, in contrast to the unalloyed Al_2O_3 film, where α-Al_2O_3 is the dominating phase at an annealing temperature of 1100 °C, the α-Al_2O_3 formation is significantly restrained for Si additions of 2 at.-% and 0.7 at.-%.

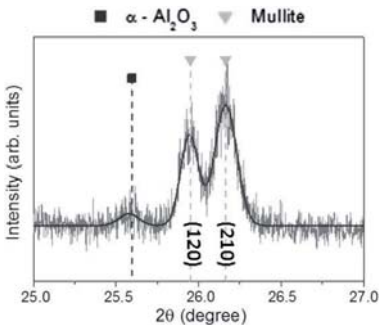

Fig. 17: High resolution X–ray diffractogram (2θ range of 25 – 27°) of the 2 at.-% Si alloyed alumina thin film after annealing at 1300°C in air.

The apparent differences in thermal stability of the unalloyed and Si alloyed alumina thin films upon annealing indicate a restraining effect of Si on crystallization and transformation sequence of the alloyed alumina thin films. Fig. 18 summarizes the transformation sequences of the post-annealing experiments of the Si containing alumina thin films in comparison to the unalloyed Al_2O_3 film.

As it can be seen, the α-Al_2O_3 phase formation temperatures are obviously higher upon Si alloying. Furthermore, the transition sequence of γ- to δ- and θ-Al_2O_3 is restrained by 100°C with respect to the unalloyed Al_2O_3 film. The formation of orthorhombic mullite at temperatures ≥ 1300°C suggests the presence of a residual amorphous silica phase in addition to the crystalline δ- and θ-Al_2O_3 phases at temperatures < 1300°C [112].

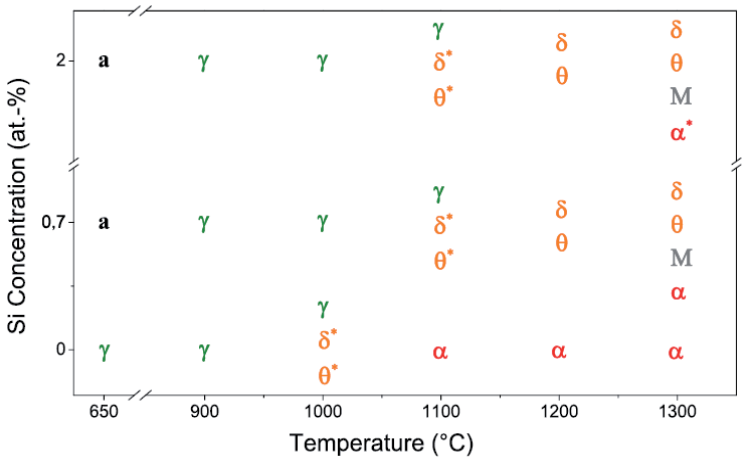

Fig. 18: Transformation sequences of Si alloyed alumina thin films compared to the transformation sequence of unalloyed Al_2O_3 thin film. (*) marks phases only detected in traces.

4.1.4.2 Effect on the chemical states

To unravel the structure evolution mechanisms, the chemical states of the unalloyed and alloyed alumina film with 2 at.-% Si were investigated by XPS as function of the annealing temperature (Fig. 19). The alloyed alumina thin film with 0.7 at.-% Si, due to a low signal to noise ratio, did not allow for a meaningful measurement of the Si (2p) binding energy. High

resolution scans were performed for the Al (2p) line of the unalloyed Al_2O_3 film and for the Al (2p) and the Si (2p) lines of the 2 at.-% Si alloyed alumina thin film.

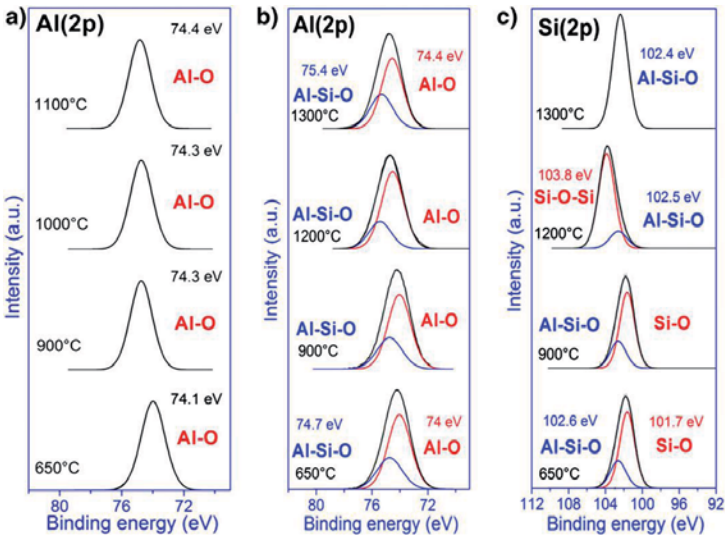

Fig. 19: Al (2p) line of the unalloyed Al_2O_3 film and b) Al (2p) and c) Si (2p) lines of the 2 at.-% Si alloyed alumina thin film as a function of annealing temperature.

Fig. 19a shows the Al (2p) line of the unalloyed Al_2O_3 film as a function of the annealing temperature. At 650°C, the Al (2p) line at 74.1 ± 0.1 eV is in good agreement with the binding energy of Al (2p) reported for γ-Al_2O_3 with binding energies of 73.3 – 74.7 eV [113] - [115]. As the annealing temperature is increased to 1100°C, the Al (2p) line is shifted by + 0.3 eV. Based on the XPS data of Wagner et al. [114] this binding energy difference is consistent with the phase formation of α-Al_2O_3 as observed here by XRD, see Fig. 10 and 11.

The Al (2p) line of the as-deposited 2 at.-% Si alloyed alumina thin (Fig. 19b) exhibits a binding energy of 74.1 ± 0.1 eV and a full width half maximum (fwhm) of 2.2 eV compared to 1.8 eV for the unalloyed film. The fwhm of the Al (2p) line allowed for a deconvolution into a high energy (HE) and low energy (LE) component with binding energies of 74.7 and 74 eV and fwhm of 1.9 eV, respectively. Based on previously published XPS data, the identified binding energy of the HE component is consistent with the formation of Al-Si-O bonds [114], [116], [117]. Furthermore, the LE component indicates the presence of Al-O bonds reported for γ-Al_2O_3 [113] - [115]. Annealing of the sample to 1300°C shifts the binding energies of the HE and LE component to 75.4 and 74.4 eV, respectively. The binding energy of the HE component corresponds to the binding energy reported for mullite bonds [114], [116], [117] and the binding energy of the LE component to α-Al_2O_3 [115], which is consistent with the XRD data shown in Fig. 17.

The formation of Al-Si-O bonds in the as-deposited state is also consistent with the results obtained for the Si (2p) line as shown in Fig. 19c. The as-deposited sample exhibits an envelope binding energy of 101.8 eV for the Si (2p) line. A deconvolution of the Si (2p) line results in a high and low energy component with binding energies of 102.6 and 101.7 eV, respectively. Similar to the Al (2p) line the HE component suggests the presence of Al-Si-O bonds reported with binding energies in the range of 102.9 - 103.3 eV [114], [116], [118], [119]. The binding energy of the LE component is increased to 103.8 eV after annealing to 1200°C, which is indicative for the oxidation of the as-deposited SiO phase to SiO_2 (103.3 – 104 eV). At 1300°C no deconvolution of the Si (2p) line with a fwhm of 1.9 eV is possible and only one component with a binding energy of 102.4 eV is exhibited. This component can be assigned to the formation of mullite also observed by XRD analysis at this

annealing step, as shown in Fig. 17. The presence of two populations of Si-O bonds in addition to the formation of Al-Si-O bonds observed for the Si (2p) line in the as-deposited state is consistent with the segregation of intergranular SiO_2 (as schematically shown in Fig. 3a and c) and is not consistent with the substitution of Si in the alumina lattice (Fig. 3b): While the formation of Si-O-Al bonds is compatible with both notions, the presence of Si-O-Si bonds is only consistent with the notion of Si-O segregation. A random, homogeneous distribution of Si in the alumina grains with a Si concentration of 2 at.-% is inconsistent with the fact that the Si 2p XPS signal comprises a significant Si-O-Si contribution.

4.1.4.3 Effect on the crystallite growth

To establish if 0.7 and/or 2 at.-% Si additions suffice to decorate the grain boundary of a 12 nm wide γ-Al_2O_3 grain the following procedure was employed.The diameter of the γ-Al_2O_3 grain was taken to be 12 nm based on the maximum grain size of 12 nm which favors the γ-Al_2O_3 formation reported by McHale et al. [51] for bulk and Rosen et al. [59] for thin films. The number of Al_2O_3 formula units contained in a 12 nm γ-Al_2O_3 grain was calculated by

$$n_{Al_2O_3} = 32 * \frac{V_1}{V_{UC_1}} = 32 * \frac{\frac{4}{3} * \pi * r_1^3}{V_{UC_1}} = 18876, \qquad \text{Eq. 7}$$

with V_1 as the volume of a Al_2O_3 grain with a radius of r_1 = 6 nm and V_{UC1} =1.5338 nm^3 as the volume of the γ-Al_2O_3 unit cell consisting of 32 formula units Al_2O_3 [120].

The number of SiO_2 formula units contained in the volume difference V_2-V_1 was calculated by following approach:

$$n_{SiO_2} = 3 * \frac{\Delta V}{V_{UC_2}} = 3 * \frac{V_2 - V_1}{V_{UC_2}} = 3 * \frac{\frac{4}{3} * \pi * r_2^3 - \frac{4}{3} * \pi * r_1^3}{V_{UC_2}} = 1304, \qquad \text{Eq. 8}$$

where V_2 is the volume of Al_2O_3 grain with a radius of $r_2 = r_1 + a$ (assuming a SiO_2 monolayer with a roughly estimated interplanar distance of a = 0.115 nm) and V_{UC2} = 0.122 nm^3 (the volume of SiO_2 unit cell consisting of 3 units SiO_2) [120].

The concentration of SiO_2 x_{SiO2} was then estimated from the number of SiO_2 and Al_2O_3 formula units to be:

$$n_{SiO_2} = \frac{n_{SiO_2}}{n_{Al_2O_3} - n_{SiO_2}} = 6.5 mol - \% \qquad \text{Eq. 9}$$

This result suggests that 0.7 and 2 at.-% SiO_2 only partially cover a 12 nm wide γ-Al_2O_3 grain. However, it is conceivable that Si-O partially covering the grain boundaries as depicted schematically in Fig. 3c may impede mass transport along the grain boundaries.

The crystallite size of the different evolving alumina and aluminosilicate phases during annealing were estimated with the Debye-Scherrer formula. Fig. 20 shows the estimated crystallite size as a function of the annealing temperature for all films studied here. Since the as-deposited alumina films with 0.7 and 2 at.-% Si addition are X-ray amorphous, the grain sizes of the alloyed and unalloyed films are compared from 900°C to 1300°C. Furthermore, crystallite sizes were not estimated for the unalloyed film at 1000°C and for

the Si alloyed films at 1100°C since the overlapping of γ-/ δ- and θ-Al_2O_3 peaks did not allow for a meaningful analysis. As shown in Fig. 20, the crystallite size of the γ-Al_2O_3 phase of the unalloyed film is estimated to be 6 nm in the as-deposited state (650°C). Upon annealing of the unalloyed Al_2O_3 at 900°C, the crystallite size of the γ-Al_2O_3 phase does not change significantly. At 1000°C no evidence for α-Al_2O_3 was observed, while further annealing to ≥ 1100°C leads to a drastic increase in crystallite size: 47 nm α-Al_2O_3 crystals are formed, according to the constitution data presented in Fig. 10. In contrast to this, the addition of Si leads to a restrained growth of alumina crystallites. At 900°C the 0.7 and 2 at.-% Si alloyed alumina films exhibit γ-Al_2O_3 crystals with a size of 4 to 5 nm. Annealing of the samples to 1000°C does not change the crystallite size of the γ-Al_2O_3 significantly. At 1200°C the 0.7 at.-% Si alloyed alumina film exhibits δ- and θ-Al_2O_3 crystallites with a size of 13 and 4 nm, respectively. For the 2 at.-% Si alloyed alumina film the size of δ- and θ-Al_2O_3 crystallites at 1200°C is estimated to be 11 and 8 nm, respectively. Further annealing of the alloyed films leads to an increase of δ- and θ-Al_2O_3 crystallites size to 12 and 7 nm for 0.7 at.-% Si and to 12 and 13 nm for the 2 at.-% Si addition, respectively. Furthermore, both Si alloyed films exhibit additional α-Al_2O_3 and mullite formation as discussed in the XRD section at 1300°C. The α-Al_2O_3 and mullite crystals of the 0.7 at.-% Si alloyed alumina film exhibit a crystallite size of 40 nm for both phases and 62 nm α-Al_2O_3 and mullite crystals for 2 at.-% Si alloying. These results suggest that the addition of Si restrains crystallite growth of the alloyed Al_2O_3 films during synthesis. Furthermore, it appears that alloyed films require larger temperatures to form δ-, θ-, and α-Al_2O_3 during the post-annealing treatment. The observed enhancement of the thermal stability of the metastable alumina phases can be understood based on kinetics:

The presence of silica at the grain boundaries may kinetically constrain grain growth, and thereby delay phase transitions.

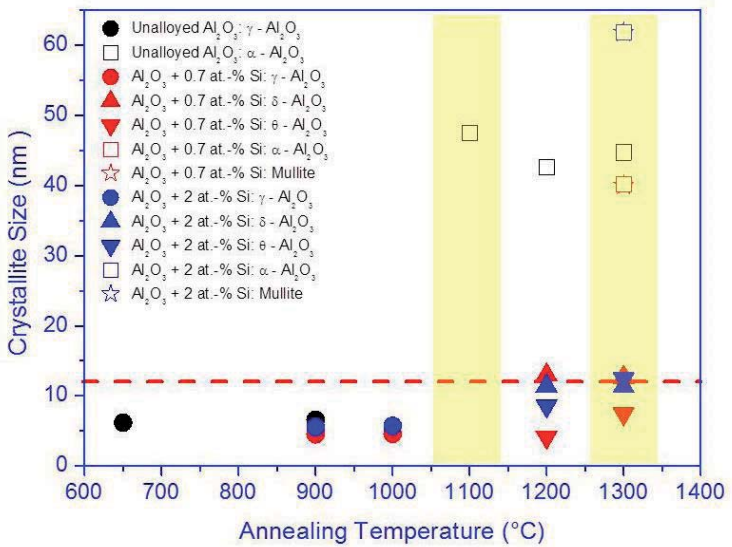

Fig. 20: Estimated crystallite size of the unalloyed Al_2O_3 film and the Si alloyed alumina films as a function of annealing temperature. The horizontal dashed line indicates the maximum grain size of 12 nm which favors the metastable γ-Al_2O_3 formation as reported by McHale et al. [51] for bulk and Rosen et al. [59] for thin films. The yellow shaded areas indicate the formation of the α-Al_2O_3 phase.

This notion is consistent with the XPS data where the presence of Al-Si-O bonds and Si-O bonds is observed, as discussed above in detail. The observed relationship between the phase formation temperatures and the crystallite sizes of the here studied alumina films with and without Si alloying can be rationalized based on a thermodynamic stabilization argument put forward by McHale et al. [51]. They report that nanocrystalline γ-Al_2O_3

powder is thermodynamically stable with respect to α-Al_2O_3 at surface areas greater than 100 square meters per gram [51]. They prove that the stabilization is caused by the smaller surface energy of γ- compared to α-Al_2O_3. Based on the data by McHale et al. [51] the maximum grain size which favors the γ-Al_2O_3 formation was estimated to be 12 nm by Rosen et al. [59]. Furthermore, this was found to be consistent with the constitution data obtained for nanostructured alumina thin films grown by filtered cathodic arc [59]. In this context the above presented notion of intergranular SiO_2 impeding mass transport and thereby restraining the grain growth of γ- and θ-Al_2O_3 and the formation of α-Al_2O_3 adds a kinetics perspective to the energetics argument of McHale et al. [51]. Based on the energetics argument of McHale et al. [51] together with the kinetics argument put forward here, the observed relationship between the phase formation temperatures and the crystallite sizes can be understood. Consequently, the observed Si induced changes in phase formation, bonding and crystallite size upon annealing are consistent with the notion that the presence of intergranular SiO_2 impedes mass transport and thereby restrains crystallization. Particularly the XPS Si (2p) data are not consistent with the competing configuration proposal where Si is substituting Al in the alumina lattice.

4.2 The effect of Y on the phase stability of Al_2O_3 polymorphs

4.2.1 Introduction

Theoretical and experimental data suggest that Y alloying of the metastable γ-Al_2O_3 phase is an effective strategy to enhance the thermal stability and to restrain the α-Al_2O_3 phase formation: Maglia et al. [79] performed atomistic simulations based on pair-wise interatomic potentials to study the energetics of trivalent cation incorporation with a concentration of 1.56 at.-% for additives such as Ga^{3+}, Fe^{3+}, Lu^{3+}, Y^{3+} in γ-Al_2O_3. The results suggested enhanced solubility of the trivalent cations in the γ-Al_2O_3 structure with respect to α-Al_2O_3, indicating phase separation and grain boundary segregation during the γ- to α-Al_2O_3 transformation. In addition, formation of trivalent cation and aluminium vacancy defect clusters located at first neighboring cation sites were proposed to restrain the γ- to α-Al_2O_3 transformation. The authors suggested that the formation of defect clusters may affect aluminum migration in the vicinity of the cation vacancies and, thereby, hinder the γ- to α-Al_2O_3 transition.

Jiang et al. [27] studied the effect of Y incorporation for two configurations of γ-Al_2O_3, cubic spinel and tetragonal hausmannite, on the relative stability of the alloyed γ-Al_2O_3 phases with respect to the alloyed α-Al_2O_3 phase. For the spinel configuration the energetic difference between the Y alloyed γ-Al_2O_3 and α-Al_2O_3 phase was reported with - $1x10^{-1}$ meV/atom and for the hausmannite configuration with - 4.2 meV/atom. The experimental investigation of the γ- to α-transition for Y alloyed Al_2O_3 was thereby proposed as a key experiment to support one of the two structure proposals of the γ-Al_2O_3 structure. However, these data are based on the assumption that Y is incorporated into the γ-Al_2O_3

and α-Al_2O_3 structures. In contrast to this, experimental studies indicate precipitation of Y as $Y_3Al_5O_{12}$ (YAG) or other intermediate yttrium aluminate phases at the grain boundaries of the alumina matrix and only a low solubility of < 10 ppm in the α-Al_2O_3 structure [61]. The effect of Y on the γ- to α-transition appears to be alloy concentration dependent: 4.2% of Y addition resulted in a delay of the metastable θ- to α-Al_2O_3 phase transformation [121], whereas for an Y concentration of 0.39 % an acceleration of the α-Al_2O_3 phase formation was observed [64]. It has been proposed that Y may affect the properties of metastable alumina phases [66] and their transformation into α-Al_2O_3 by microstructural effects such as by availability of additional sites for heterogeneous nucleation of the oxide [66] as well as hampering the grain growth of metastable alumina phases [66]. A possible explanation for these controversies is proposed by Jedliński et al. [66]. The authors surmised that a small Y content accelerates the transformation while a relatively high Y additive concentration to alumina-forming alloys may restrain the transformation. However, the authors did not report concentration limits which define the accelerating/retarding transformation effect of Y. Thus, on the basis of the afore mentioned contradictive results, the solubility of Y in the γ-Al_2O_3 structure and the effect of Y on the stability of the metastable Al_2O_3 phases with respect to α-Al_2O_3 at different concentrations is yet not fully understood. Within this study we, therefore, explore the effect of up to 7.5 at.-% Y addition on the stability of Al_2O_3 using density functional theory and post-annealing of Y alloyed alumina thin films deposited by filtered cathodic arc.

Furthermore, additional experiments were performed with the focus on the low temperature synthesis of yttrium aluminates. The Y_2O_3-Al_2O_3 binary system exhibits several ternary phases such as the $Y_3Al_5O_{12}$ and $YAlO_3$ phases, commonly referred to as

yttrium aluminum garnet and yttrium aluminum perovskite phase, respectively [122]. Among these phases, the $Y_3Al_5O_{12}$ phase, which defines the end-member within the Al_2O_3-Y_2O_3 system, exhibits excellent chemical stability [123], high creep resistance [123] - [125], low oxygen diffusivity of 10^{-20} to 10^{-25} W m^{-1} K^{-1} [126] , as well as a high thermal expansion coefficient [126] and excellent phase stability [126], [125]. Owing to these properties the $Y_3Al_5O_{12}$ phase is used for wide range of applications: Apart from its general application areas as solid state laser host [127], [128] and scintillation material [129], the $Y_3Al_5O_{12}$ phase is extensively used as eutectic $Al_2O_3/Y_3Al_5O_{12}$ composite material with enhanced flexural strength in high-efficiency power-generation [130] and was recently also considered as a potential alternative for thermal barrier coatings commonly based on yttria-stabilized zirconia [126]. Apart from the $Y_3Al_5O_{12}$ phase, the $YAlO_3$ phase in combination with rare earths such as Ce [131], [132] and Pr [133] exhibits very good mechanical and chemical stability, a broad emission spectrum with 370 nm and a scintillation decay time of 27 ns promoting a high light yield as well as fast scintillation which makes it a useful material for solid state lasers and scintillators [131] - [133]. The solid state synthesis of the $Y_3Al_5O_{12}$ and $YAlO_3$ phases is reported by wet chemical processing [134], metal-organic preceramic processing [135], yttrium carboxylate-alumoxane route [136] requiring synthesis temperatures in the excess of 1100°C for $YAlO_3$ and 1600°C for $Y_3Al_5O_{12}$ [137], [138]. Recently, the synthesis of single phased, polycrystalline $Y_3Al_5O_{12}$ has been reported by sol-gel processing at temperatures of 800°C [134], [139]. However, wet chemical processing strategies are generally based on the following sequential processing steps: Deposition, drying and sintering. Due to large changes in equilibrium volume between the so initiated phase transformations, this may not only restrict the achievable film thickness without crack formation below 0.1 µm for

ceramic sol gel films [140] but may also present significant challenges for a high rate deposition scale up of this approach. Furthermore, the use of expensive and hazardous alkoxides precursors may present a drawback from an industrial processing point of view. Therefore, alternative and direct synthesis methods, such as physical vapor deposition may allow the deposition of $Y_3Al_5O_{12}$ thin films with high thickness and quality at lower synthesis temperatures. Deposition of 5.5%Gd:$Y_3Al_5O_{12}$ thin films on Si(100) substrates at 700°C and – 100 V substrate bias by using rf-magnetron sputtering was reported by Deng et al. [141]. However, crystallization of the as-deposited amorphous samples was only achieved after annealing of the Gd:$Y_3Al_5O_{12}$ thin films at 1000°C for 10h. Bai et al. [142] reported the synthesis of epitaxial single crystalline pure YAG thin films with a deposition rate of 50 – 80 Å/min on (111) gadolinium gallium garnet substrates at 1000°C by using metalorganic chemical vapor deposition.

Therefore, within this study we investigate the effect of different Y concentrations on the phase formation of thin films grown by filtered cathodic arc. The formation of $YAlO_3$ and $Y_3Al_5O_{12}$ at Y concentrations ≥ 1.9 at.-% was observed in an amorphous matrix at a synthesis temperature of 650 °C with a deposition rate of 1500 Å/min on Si(100) substrates, indicating that ion bombardment by film forming species provides a pathway to low temperature synthesis of these ternary phases.

4.2.2 Ab initio study on the effect of Y on the phase stability of γ- and α-Al_2O_3

The energy of solution $E_{sol,Y\ (\gamma,\gamma)}$ and $E_{sol,Y\ (\alpha,\alpha)}$ for addition of Y in γ-Al_2O_3 and α-Al_2O_3 is displayed in Fig. 21.

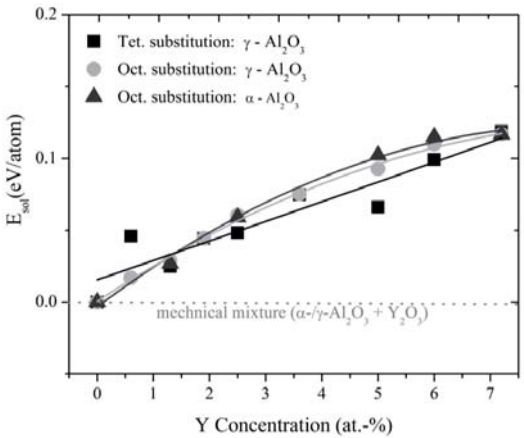

Fig. 21: $E_{sol,Y\ (\gamma,\gamma)}$ for tetrahedral and octahedral substitution by Y in γ-Al_2O_3 and $E_{sol,Y\ (\alpha,\alpha)}$ for octahedral substitution in α-Al_2O_3. The mechanical mixture of α-/γ- Al_2O_3 and Y_2O_3 is represented by the dotted line.

The calculated data are fitted with a second order polynomial function as guide for the eye. The positive energies of solution E_{sol} exhibit a trend towards increasing energy values for all calculated substitution sites in the γ- and α-phase. The increasing E_{sol} suggests decreasing chemical stability of the compounds with increasing Y concentration. Thus, a decomposition into the stable compounds α-/ γ-Al_2O_3 and Y_2O_3 is be energetically favored upon Y addition.

4.2.3 The effect of Y additives on the phase formation of Al_2O_3 thin films deposited by filtered cathodic arc

4.2.3.1 Chemical composition

The chemical composition of the as-deposited samples was measured by using EDX analysis. All samples revealed a stoichiometric oxygen to metal ratio of 1.5 and a Y concentration of 0, 0.8, 1.4 and 4.0 at.-% Y. Additional EXD analysis of the Al-Y cathodes after deposition exhibited a deviation of $\leq \pm$ 0.5 at.-% from the initial Y concentration of the Al-Y cathode before deposition.

4.2.3.2 Thermal stability of Y alloyed alumina thin films

Fig. 22 and 23 display the X – ray diffractograms of the unalloyed and Y alloyed alumina thin films in the as-deposited state and after annealing at temperatures in the range of 800 - 1200°C. Fig. 22a and 23 show the XRD analysis of the unalloyed Al_2O_3 thin film.

At 650°C and 800°C, the Al_2O_3 thin film exhibits only peaks characteristic for γ-Al_2O_3. At annealing temperatures ≥ 900°C, additional traces of θ-Al_2O_3 cannot be excluded. At 1100°C α-Al_2O_3 dominates the X-ray diffractogram. The 0.8 at.-% Y alloyed alumina thin film exhibits the presence of γ-Al_2O_3 in the as-deposited state (Fig. 22b and 23). Furthermore, the higher intensity of the hump in the 2θ range of 20 – 40°, as well as splitting of the (440) γ-Al_2O_3 peak and the shoulder left to the (400) γ-Al_2O_3 peak indicate the presence of a residual Y_2O_3 or $Y_3Al_5O_{12}$ phase. After annealing to 1000°C, the additional formation of θ-Al_2O_3 traces cannot be excluded. The γ-/θ-Al_2O_3 and

$Y_2O_3/Y_3Al_5O_{12}$ phase mixture remains stable up to 1200°C. At 1200°C, the $Y_3Al_5O_{12}$ phase fraction is observed to increase significantly. As the $Y_3Al_5O_{12}$ peaks overlap with the α-Al_2O_3 peaks the presence of the α-phase traces cannot be excluded.

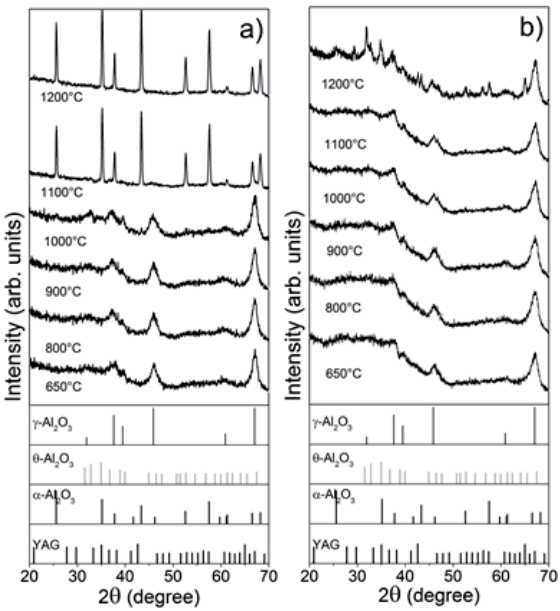

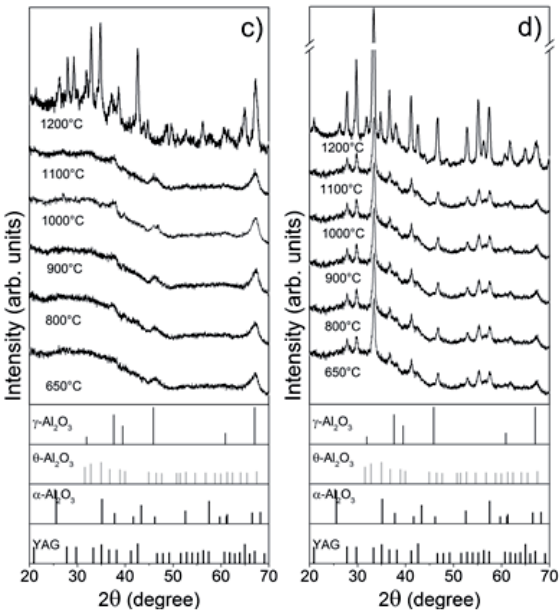

Fig. 22: X-ray diffractograms of the unalloyed and Y alloyed alumina thin films deposited at floating bias potential as function of the annealing temperature. a) Unalloyed Al_2O_3 thin film, b) 0.8, c) 1.4 and d) 4 at.-% Y alloyed alumina thin films.

The 1.4 at.-% Y alloyed alumina thin film exhibits the presence of γ-Al_2O_3 and Y_2O_3 phase mixture in the as-deposited state and a similar enhanced stability of the metastable alumina phase up to 1200°C (Fig. 22c and 23). At 1200°C, additional peaks which can be assigned to the $Y_3Al_5O_{12}$ phase and traces of the α-Al_2O_3 phase are observed. The alumina thin film alloyed with 4.0 at.-% Y exhibits $Y_3Al_5O_{12}$ formation already in the as-deposited state with some traces of γ-Al_2O_3 (Fig. 22d). This phase mixture is maintained up to ≤ 1100°C. At ≤ 1200°C, additional traces of α-Al_2O_3 are observed.

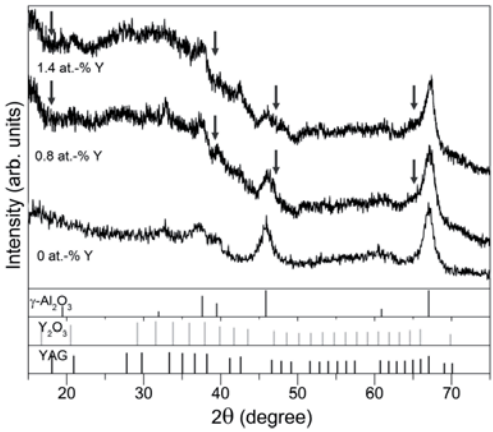

Fig. 23: X-ray diffractograms of the unalloyed and 0.8 and 1.4 at.-% Y alloyed alumina thin films deposited at floating bias potential. The arrows indicate the area of possible Y_2O_3 and/or $Y_3Al_5O_{12}$ traces.

Summarizing, the phase evolution of the 0.8 and 1.9 at.-% Y alloyed thin films (Fig. 24) indicate a restrained γ- to α-Al_2O_3 phase transformation and, hence, an enhanced stability of the metastable alumina phases. Thereby, we report evidence that even low Y concentrations of 0.8 at.-% restrain the γ- to α-Al_2O_3 phase transformation and do not promote an accelerating effect on the α-Al_2O_3 phase formation, as proposed by Jedliński et al. [66]. Furthermore, all Y alloyed alumina thin films exhibit the formation of the $Y_3Al_5O_{12}$ phase at 1200°C while Y alloying at 4.0 at.-% already leads to the formation of $Y_3Al_5O_{12}$ in the as-deposited state. The presence of other yttrium aluminate phases, such as $YAlO_3$ (yttrium aluminum perovskite) or residual Y_2O_3 traces cannot be excluded upon annealing at 1200°C for all Y alloyed samples as precise identification of these phases is not possible due to peak overlapping with the Al_2O_3 and $Y_3Al_5O_{12}$ peaks.

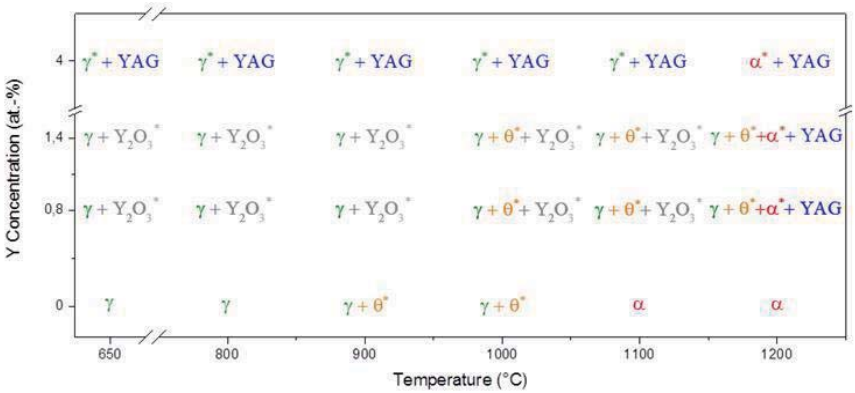

Fig. 24: Phase evolution of unalloyed and Y alloyed alumina thin films as function of temperature. Star indexing indicates phases only observed in traces.

The theoretically and experimentally obtained lattice parameters of the unalloyed and Y alloyed γ-Al_2O_3 phases were compared (Fig. 25). Ab initio data suggest that the substitution of Al by Y in the γ-Al_2O_3 structure in the range of 0.6 to 7.5 at.-% exhibits an increase in lattice parameter for both, tetrahedral and octahedral substitutions. In contrast to the calculated lattice parameter, the experimentally obtained data do not indicate a significant change in lattice parameter. These diffraction data prove that Y is not incorporated in the γ-Al_2O_3 structure. Thus, Y alloying of the γ-Al_2O_3 thin films appears to cause decomposition into the stable compounds α-/ γ-Al_2O_3 and Y_2O_3 as predicted by the here presented ab initio data. This notion is furthermore consistent with the phase formation data reported above.

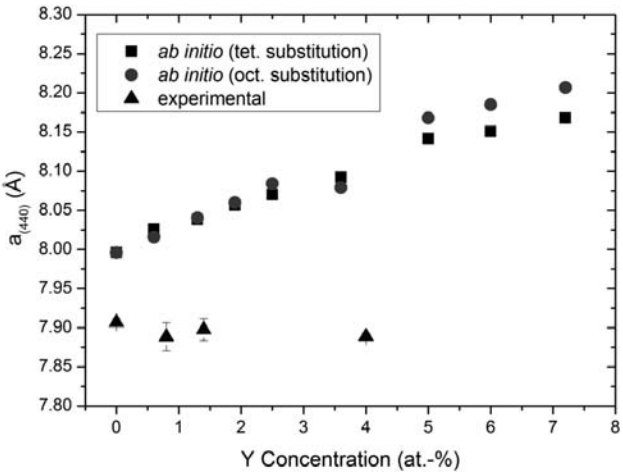

Fig. 24: Measured and calculated γ-Al_2O_3 lattice parameter as function of the Y concentration.

To elucidate the underlying mechanism of the restrained phase transitions, crystallite size estimation of the unalloyed and Y alloyed alumina thin films was performed as function of the annealing temperature. The crystallite size was estimated by using the Debye-Scherrer- Equation [100].

Fig. 26 shows the estimated crystallite size as function of the annealing temperature. The 4 at.-% Y alloyed alumina thin film was not taken into account because the overlapping peaks of $Y_3Al_5O_{12}$ and the alumina phases did not allow for a meaningful peak fitting. The unalloyed Al_2O_3 thin film exhibits a crystallite size of approximately 7 nm at temperatures ≤ 1000°C while the formation of α-Al_2O_3 at ≤ 1100°C results in a crystallite size to 29 nm. Y addition, however, results in the formation of $Y_3Al_5O_{12}$ at 1200°C with a crystallite size of 20 nm. As the θ- and α-Al_2O_3 phase were only observed in traces, a meaningful peak broadening analysis of the θ- and α-Al_2O_3 phases was not possible. The crystallite size of

the γ-Al_2O_3 phase of the 0.8 at.-% Y alloyed alumina thin film changes from 6 to only 10 nm upon annealing to 1200°C, while the with 1.4 at.-% Y alloyed alumina thin film exhibits an increase of the γ-Al_2O_3 crystallite size from 3 to 12.5 nm. Nahif et al. [143] recently investigated the effect of Si additions on the stability and grain size of alumina thin films and observed prior to the formation of the α-phase and Mullite a maximum grain size of the unalloyed and alloyed γ-Al_2O_3 phase of 12 nm. Interestingly, this is the maximum grain size that was estimated by Rosen et al. [59] based on energetics data presented by McHale et al. [51] rendering the γ-Al_2O_3 more stable than the α-phase. The authors showed that Si additions stabilize the metastable alumina polymorphs and argue that this can be understood based on considering energetics based on McHale's et al. [51] as well as the presence of Si at the grain boundaries impeding mass transport.

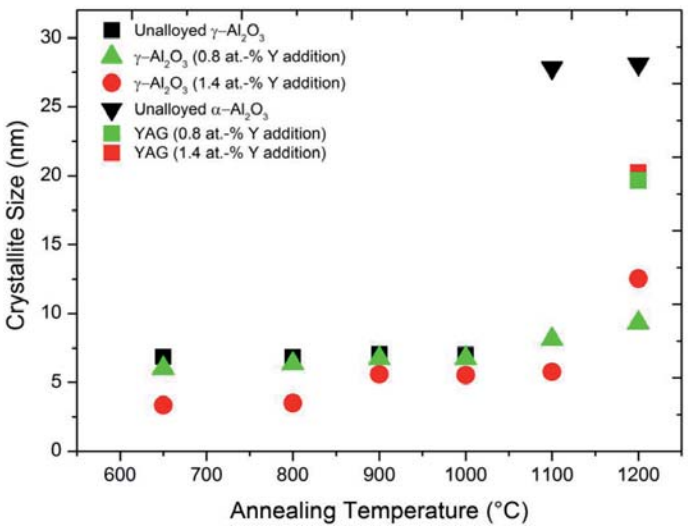

Fig. 25: Estimated crystallite size of the unalloyed and the Y alloyed alumina thin films with 0.8 and 1.4 at.-% Y deposited at floating bias potential as function of the annealing temperature.

The Y alloyed Al_2O_3 thin films investigated here show – just as the Si alloyed Al_2O_3 thin films discussed above – a stabilization of the γ-Al_2O_3. Also here the maximum experimentally observed grain size of 12.5 nm is consistent with the stability proposal for γ-Al_2O_3 by McHale's et al. [51].

Based on the ab initio data predicting decomposition of the γ-$(Al,Y)_2O_3$ solid solution and the unaltered lattice parameter of the γ-Al_2O_3 phase upon Y addition, it is suggested that Y is not incorporated into the γ-phase. Instead Y may reside at the grain boundaries. Thereby, Y may effectively restrain grain boundary mobility and growth of the Al_2O_3 crystallites and, thus, enhance the stability of the metastable γ-Al_2O_3 phase by kinetically hindering α-Al_2O_3 phase formation.

4.2.3.3 Low temperature synthesis of $Y_3Al_5O_{12}$ by using filtered cathodic arc technique

4.2.3.4 Chemical composition

EDX analysis of the as-deposited samples revealed stoichiometric oxygen to metal ratios of 1.5 and Y concentrations of 0, 1.9, 3.5 and 7.0 at.-%. EDX analysis of the Al-Y cathodes after deposition revealed a deviation of $\leq \pm 0.5$ at.-% from the initial Y concentration of the Al-Y cathode before deposition.

4.2.3.5 Phase constitution and morphology

Fig. 27 displays the X – ray diffractograms of the thin films deposited at 650°C and – 130 V substrate bias potential. The Al_2O_3 thin film without Y addition exhibits only peaks characteristic for γ-Al_2O_3 in the as-deposited state, which is in good agreement with previously published results [143]. The Al_2O_3 thin film with a concentration of 1.9 at.-% Y exhibits a low intensity diffraction peak at 26.8° which can be attributed to the presence of the $YAlO_3$ phase. Additional traces of γ-Al_2O_3 are indicated by the hump at 66.8°. In contrast to this, the increase of Y concentration up to 3.5 at.-% results in the formation of traces of $Y_3Al_5O_{12}$ and $YAlO_3$ in the as-deposited state, as observed by the diffraction peaks at 26.8° and 33.3°. At 7 at.-% Y addition the $Y_3Al_5O_{12}$ phase is dominating the X-ray diffractogram. However, the presence of an additional $YAlO_3$ phase is indicated by the diffraction peak at 26.8°. According to the highest yttrium concentration used within this study, the $Y_3Al_5O_{12}$/ Al_2O_3 ratio is estimated to be ¼ for the 7 at.-% Y alloyed Al_2O_3 thin film which suggests that the presence of residual alumina phases cannot be excluded.

However, as the $Y_3Al_5O_{12}$ peaks in the X-ray diffractograms strongly overlap with peaks of the alumina polymorphs a meaningful peak assignment of the residual alumina phase is not possible.

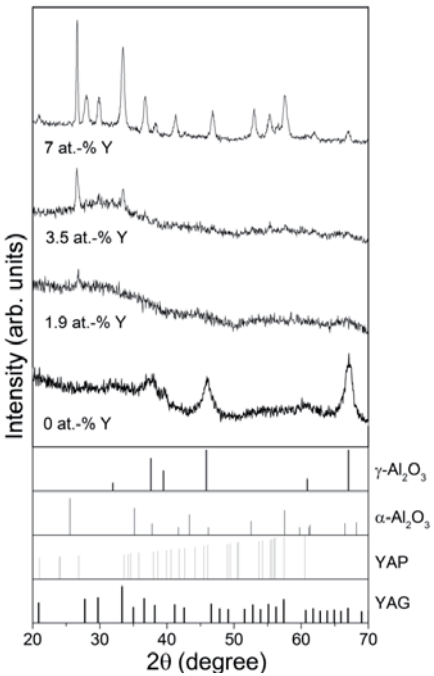

Fig.27: X-ray diffractograms of the unalloyed and Y alloyed alumina thin films deposited at 650°C and – 130 V substrate bias potential as function of the Y concentration.

Furthermore, Y addition ≥ 3.5 at.-% promotes the formation of precipitates which are distributed across the thin film cross-section, as shown by the cross-sectional TEM BF image of the thin film with 7 at.-% Y addition (Fig. 28). The matrix area exhibits an elemental concentration of 59 - 60 at.-% O, 32 – 35 at.-% Al and 6 – 8 at.-% Y, whereas

an elemental concentration of 52 – 54 at.-% O, 39 – 40 at.-% Al and 6 – 9 at.-% Y can be assigned to the precipitates. With reference to the compositions of $Y_3Al_5O_{12}$ containing 60 at.-% O, 25 at.-% Al and 15 at.-% Y and of $YAlO_3$ with 60 at.-% O, 20 at.-% Al and 20 at.-% Y the presence of excess Al_2O_3 appears reasonable.

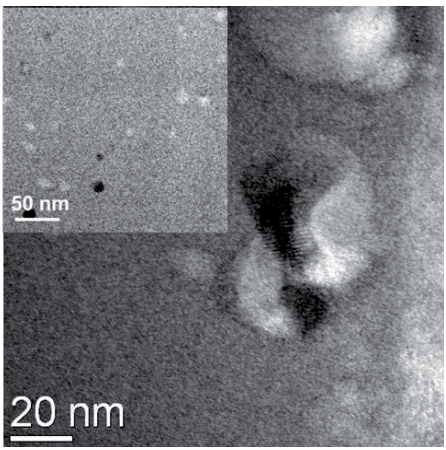

Fig. 28: TEM BF image of the cross-section of a thin film with 7 at.-% Y addition showing precipitate formation. The inset figure displays the cross-sectional TEM BF image of the precipitate formation across the cross-section of the thin film with 7 at.-% Y addition.

The formation of Y-Al-O precipitates upon Y alloying of alumina is consistent with Gülgün et al. [144], [145]. The authors reported the formation of $YAlO_3$ precipitates before or in addition to $Y_3Al_5O_{12}$ precipitates for hot-pressed Y doped α-Al_2O_3 upon alloying with 2000 ppm of Y at a synthesis temperature of 1450 - 1600°C.

Fig. 29 shows the cross-sectional TEM BF image of the thin film with 7 at.-% Y and SAD analysis of the precipitates area. Aside from the diffuse background which indicates the dominating presence of an amorphous matrix, the SAD pattern provides γ-Al_2O_3 reflections

and additional diffraction rings which can be assigned to the presence of a yttrium aluminate phase. However, as the reflections of the $Y_3Al_5O_{12}$ and $YAlO_3$ phase overlap to some extent, a precise assignment of the reflections to only one yttrium aluminate phase is not possible.

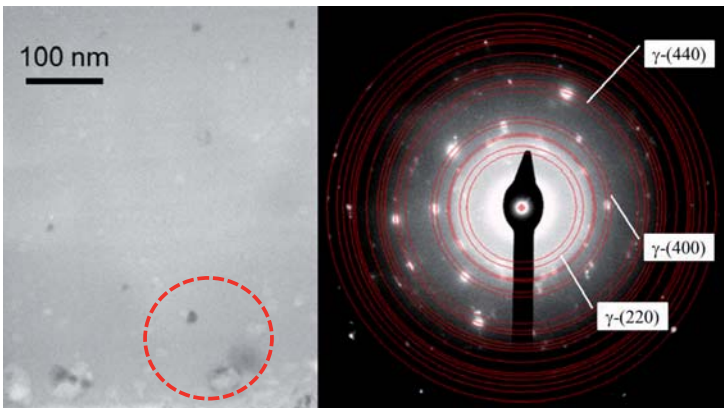

Fig. 29: Cross-sectional TEM BF image and SAD analysis of an area containing precipitates for the thin film with 7 at.-% Y addition. The red circle indicates the estimated area of analysis.

However, the presence of yttrium aluminate phases is in good agreement with the XRD data presented for the films containing 3.5 and 7 at.-% Y, which exhibited the formation of the $Y_3Al_5O_{12}$ and $YAlO_3$ phase. The presence of this yttrium aluminate precipitates may further enhance the mechanical properties of Al_2O_3 based materials [146]. Li and Gao [147] reported an increase in fracture strength and fracture toughness of about 56 and 25%, respectively, for Al_2O_3–25 vol.% $Y_3Al_5O_{12}$ nanocomposites, as compared to the reference monolithic alumina. Furthermore, and besides the significant reduction in synthesis temperature reported here, another benefit of the filtered cathodic arc synthesis technique utilized here is the comparatively high deposition rate of 1500 Å/min in

comparison to deposition rates of magnetron sputtered garnet films with 50 – 80 Å/min [142].

5. Conclusions

Using DFT, the effect of up to 5 at.% Si on the stability and electronic structure of γ- and α-Al_2O_3 has been investigated. The additives have been positioned at different substitution sites in the γ-phase. The DFT results for $(Al,Si)_2O_3$ predict a trend towards spontaneous decomposition into α-/γ-Al_2O_3 and SiO_2. The formation of the metastable γ-$(Al,Si)_2O_3$ phase can only be expected during non-equilibrium processing where the decomposition is kinetically hindered. The Si-induced changes in stability of these metastable solid solutions may be understood based on the electronic structure. Stiffer Si–O bonds are formed in the γ-phase compared to the Si–O bonds in the α-phase, rendering γ-$(Al,Si)_2O_3$ more stable than α-$(Al,Si)_2O_3$. Thereby, it has been shown that stability calculations based on an alloy element composition range in contrast to calculations based on a single alloy element composition enables the definition of stability regions. From a materials design perspective, this approach is advantageous compared to stability calculations based on a single concentration calculation. To validate the results obtained by the theoretical approach, the effect of Si additives on the phase transformation sequence and phase formation temperatures was investigated for filtered cathodic arc deposited Al_2O_3 thin films. The obtained XRD data suggest that by addition of Si the transformation of γ- to δ- and θ-Al_2O_3 is restrained by 100°C extending the thermal stability range of the δ- and θ-phase by ≥ 200°C with respect to the unalloyed Al_2O_3 thin film. The formation of α-Al_2O_3 is restrained by 200°C upon addition of Si. Furthermore, the formation of orthorhombic mullite is observed at ≥ 1300°C for the Si alloyed samples, while single phase α-Al_2O_3 is obtained for the unalloyed films at 1100°C. According to the experimentally observed stabilization of the metastable γ- to δ- and θ-Al_2O_3 phases and the restrained α-Al_2O_3 phase formation

upon Si addition, the presence of SiO_2 at the grain boundaries is suggested. SiO_2 residing at the grain boundaries may impede mass transport and hence crystallite growth, which appears to be the cause of the reported stabilization. Inconsistency of the Si bonding data obtained by XPS with the notion of a solid solution of Si in the alumina lattice suggests that this cannot serve as an explanation for the stability enhancement.

Furthermore, the effect of up to 7.5 at.-% Y addition on the phase stability of Al_2O_3 thin films has been investigated by using density functional theory and annealing of unalloyed and Y alloyed alumina thin films deposited by filtered cathodic arc. The calculations suggest spontaneous decomposition of Y alloyed γ- and α-Al_2O_3 solid solutions. This prediction is consistent with experiments: The lattice parameters of the unalloyed and Y alloyed γ-Al_2O_3 thin films are comparable and do not replicate the predicted expansion in equilibrium volume as Y is incorporated into the γ-phase. While the γ- to α-Al_2O_3 phase transition takes place T ≤ 1100°C for the unalloyed Al_2O_3 thin film, the Y alloyed Al_2O_3 films exhibit with respect to phase formation in the as deposited state and the phase evolution upon annealing significant differences: The presence of a γ-Al_2O_3, Y_2O_3 and/or $Y_3Al_5O_{12}$ phase mixture is observed in the as-deposited state. The formation of intensive $Y_3Al_5O_{12}$ peaks and traces of α-Al_2O_3 were observed at 1200°C indicating a formation at 1100°C < T ≤ 1200°C rendering the γ-Al_2O_3 phase of the Y alloyed thermally more stable than the unalloyed films. Based on the temperature induced changes in crystallite size it may be speculated that presence of Y containing phases kinetically impede mass transport and hence α-Al_2O_3 phase formation.

Fig. 30 summarizes the temperature induced changes in crystallite size for the unalloyed and Si and Y alloyed alumina thin films studied here. In this thesis experimental evidence

is presented in support of the notion that the stabilization of γ-Al_2O_3 is enabled by the presence of Si and Y at the grain boundaries constraining crystallite growth.

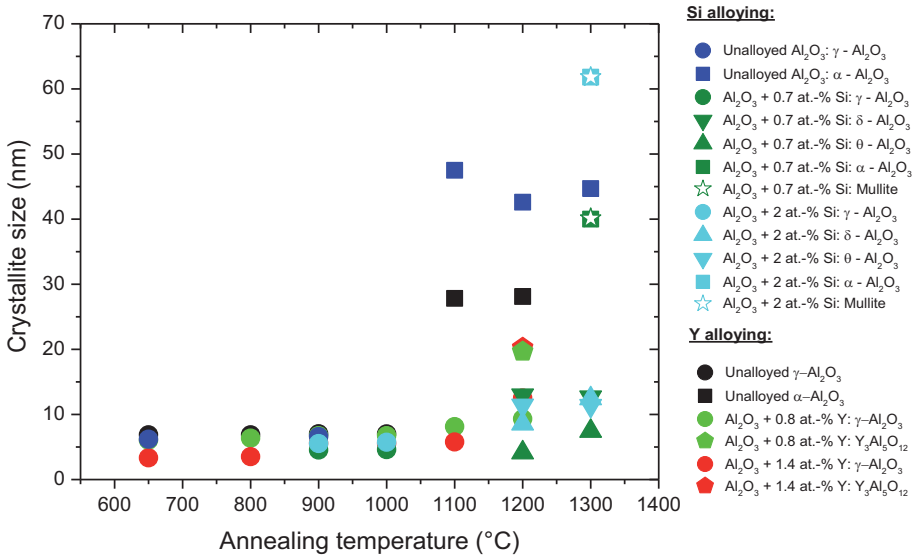

Fig. 30: Estimated crystallite size of the unalloyed and the Si and Y alloyed alumina thin films studied within this thesis as function of the annealing temperature.

In addition, the XRD data of Y alloyed Al_2O_3 thin films deposited at 650°C and – 130 V bipolar pulsed substrate bias potential indicate the formation of yttrium aluminates for a Y concentration range of 1.9 – 7 at.-% Y. With increasing Y concentration the formation of $Y_3Al_5O_{12}$ as dominating crystalline phase was observed, while the presence of a residual nanocrystalline Al_2O_3 phase appears likely for the Y alloyed Al_2O_3 thin films. The growth of $Y_3Al_5O_{12}$ phase at 650 °C highlights the potential of synthesis techniques utilizing ion

bombardment of the film forming species for low temperature synthesis as bulk synthesis of this phase is reported at 1600°C.

6. Future work

Based on the results obtained within this study, Si and Y additives appear to be promising alloying candidates to enhance the thermal stability of metastable alumina polymorphs and to extend the application temperature range thereof. Therefore, future work suggestions include deposition of alumina thin films with higher Si concentrations to investigate the presence of SiO_2 grain boundary segregation in more detail. As the increase of Si concentration may promote arc instabilities and require higher cooling rates, due to the lower melting point of the Al-Si alloy cathode, the use of separate Al and Si sources and an alternative deposition system is suggested. This can either be fulfilled by using combinatorial magnetron sputtering or establishing a hybrid deposition system consisting of the current arc source and an additional magnetron attached at the upper window flange of the vacuum chamber.

Furthermore, the suggested presence of SiO_2 at the grain boundaries may be further investigated by either additional high resolution TEM (HR-TEM) analysis or by using atom probe tomography (APT). Based on reports of the sol-gel community [74], where NaOH solution were used to preferentially leach SiO_2 in Si alloyed Al_2O_3 gels, additional synthesis of Si alloyed alumina powders for leaching experiments may be performed. Testing the phase stability of the leached Si alloyed Al_2O_3 powders by annealing experiments may further contribute to study the residing sites of Si.

Moreover, further studies on the mechanical properties of Si and Y alloyed alumina thin films are suggested to explore their potential for industrial application. Within this context the deposition of Si and Y alloyed alumina thin films on industrial substrates (e.g.

cemented carbide cutting tools) is advised as the substrate material may have a substantial influence on the morphological and structural evolution of the alloyed alumina thin films.

Furthermore, the obtained low temperature deposition of the yttrium aluminate precipitates within this study suggests to further investigate the effect of energetic bombardment on the low temperature synthesis of pure $Y_3Al_5O_{12}$ thin films. As $Y_3Al_5O_{12}$ synthesis by conventional solid state reaction methods requires high temperatures in the excess of 1600°C, alternative synthesis methods which allow for a low temperature synthesis are of key interest for a wider application of $Y_3Al_5O_{12}$ ceramics. Therefore, use of energetic bombardment during PVD synthesis may contribute towards the low temperature synthesis of the $Y_3Al_5O_{12}$ phase.

7. References

[1] S.K. Kim, C.S. Hwang, J. Appl. Phys. 96 (2004) 2323–2329.

[2] S. J. Yun, Y.-W. Ko, J.-W. Lim, Applied Physics Letters 85 (2004) 4896–4898.

[3] B. Vermang, H. Goverde, L. Tous, A. Lorenz, P. Choulat, J. Horzel, J. John, J. Poortmans, R. Mertens, Prog. Photovolt: Res. Appl. 20 (2012) 269–273.

[4] E. Fredriksson, J.-O. Carlsson, Surface and Coatings Technology 56 (1993) 165–177.

[5] X. Nie, E.I. Meletis, J.C. Jiang, A. Leyland, A.L. Yerokhin, A. Matthews, Surface and Coatings Technology 149 (2002) 245–251.

[6] B. Lux, C. Colombier, H. Altena, K. Stjernberg, Thin Solid Films 138 (1986) 49–64.

[7] G.D. Wilk, R.M. Wallace, J.M. Anthony, J. Appl. Phys. 89 (2001) 5243–5275.

[8] J. Yang, M. Li, H. Zhang, C. Gao, Rev. Sci. Instrum. 82 (2011) 45108–4.

[9] D.S. MacIver, W.H. Wilmot, J.M. Bridges, Journal of Catalysis 3 (1964) 502–511.

[10] J.F. DeWilde, H. Chiang, D.A. Hickman, C.R. Ho, A. Bhan, ACS Catal 3 (2013) 798–807.

[11] H. Knözinger, P. Ratnasamy, Catalysis Reviews 17 (1978) 31–70.

[12] C. Täschner, B. Ljungberg, I. Endler, A. Leonhardt, Surface and Coatings Technology 116–119 (1999) 891–897.

[13] J. Müller, M. Schierling, E. Zimmermann, D. Neuschütz, Surface and Coatings Technology 120–121 (1999) 16–21.

[14] J.M. Schneider, W.D. Sproul, A. Matthews, Surface and Coatings Technology 98 (1998) 1473–1476.

[15] O. Zywitzki, G. Hoetzsch, F. Fietzke, K. Goedicke, Surface and Coatings Technology 82 (1996) 169–175.

[16] D. Music, F. Nahif, K. Sarakinos, N. Friederichsen, J.M. Schneider, Appl. Phys. Lett. 98 (2011) 111908–3.

[17] K. Sarakinos, D. Music, F. Nahif, K. Jiang, A. Braun, C. Zilkens, J.M. Schneider, phys. stat. sol. (RRL) 4 (2010) 154–156.

[18] E. Wallin, T. I. Selinder, M. Elfwing, U. Helmersson, EPL (Europhysics Letters) 82 (2008) 36002.

[19] K. Jiang, K. Sarakinos, S. Konstantinidis and J. M. Schneider, Journal of Physics D: Applied Physics 43 (2010) 325202.

[20] A. Schütze, D.T. Quinto, Surface and Coatings Technology 162 (2003) 174–182.

[21] D.H. Trinh, K. Back, G. Pozina, H. Blomqvist, T. Selinder, M. Collin, I. Reineck, L. Hultman, H. Högberg, Surface and Coatings Technology 203 (2009) 1682–1688.

[22] R. Prescott, M.J. Graham, Oxid Met 38 (1992) 233-254.

[23] D.D. Ragan, T. Mates, D.R. Clarke, Journal of the American Ceramic Society 86 (2003) 541–545.

[24] Q. Wei, Z.-X. Chen, Z.-H. Wang, Y.-L. Hao, J.-X. Zou, Z.-R. Nie, Journal of Alloys and Compounds 387 (2005) 292–296.

[25] A. Douy, Journal of the European Ceramic Society 26 (2006) 1447–1454.

[26] O. Mekasuwandumrong, P. Tantichuwet, C. Chaisuk, P. Praserthdam, Materials Chemistry and Physics 107 (2008) 208–214.

[27] K. Jiang, D. Music, K. Sarakinos and J.M. Schneider, Journal of Physics: Condensed Matter 22 (2010) 505502.

[28] E. Wallin, J. M. Andersson, V. Chirita and U. Helmersson, Journal of Physics: Condensed Matter 16 (2004) 8971.

[29] I. Levin, D. Brandon, Journal of the American Ceramic Society 81 (1998) 1995–2012.

[30] R.W.G. Wyckoff (Ed.), Crystal Structures, Krieger ed., Malabar, 1982.

[31] W. Oliver, G. Pharr, Journal of Materials Research 7 (1992) 1564–1583.

[32] E. Dörre, H. Hübner, Alumina: Processing, properties, and applications, Springer, 1984.

[33] S. Toyoda, T. Shinohara, H. Kumigashira, M. Oshima, Y. Kato, Applied Physics Letters 101 (2012) 231607.

[34] U. Eritt, G. von Hayn, E. Lugscheider, D. Neuschütz, J. Müller, Mat.-wiss. u. Werkstofftech. 33 (2002) 45–51.

[35] W.H. Gitzen, Alumina as a ceramic material, Columbus: American. Ceramic Society, 1970.

[36] Y. Sato, S.-i. Akimoto, J. Appl. Phys. 50 (1979) 5285–5291.

[37] P. Chaparala, J.S. Suehle, C. Messick, M. Roush, in: Reliability Physics Symposium, 1996. 34th Annual Proceedings., IEEE International, 1996, pp. 61–66.

[38] S. Kitaoka, T. Matsudaira, M. Wada, MATERIALS TRANSACTIONS 50 (2009) 1023–1031.

[39] T. Matsudaira, M. Wada, T. Saitoh, S. Kitaoka, Acta Materialia 58 (2010) 1544–1553.

[40] G. Paglia, A.L. Rohl, C.E. Buckley, J.D. Gale, Phys. Rev. B 71 (2005) 224115.

[41] M. Sun, A.E. Nelson, J. Adjaye, The Journal of Physical Chemistry B 110 (2006) 2310–2317.

[42] G. Gutiérrez, A. Taga, B. Johansson, Physical Review B 65 (2001) 12101.

[43] G. Paglia, C.E. Buckley, A.L. Rohl, B.A. Hunter, R.D. Hart, J.V. Hanna, L.T. Byrne, Phys. Rev. B 68 (2003) 144110.

[44] E. Menéndez-Proupin, G. Gutiérrez, Phys. Rev. B 72 (2005) 35116.

[45] J.M. Knaup, C. Köhler, T. Frauenheim, A.T. Blumenau, M. Amkreutz, P. Schiffels, B. Schneider, O.-D. Hennemann, J. Phys. Chem. B 110 (2006) 20460–20468.

[46] M. Trueba, S.P. Trasatti, Eur. J. Inorg. Chem. 2005 (2005) 3393–3403.

[47] S.J. Wilson, J.D.C. Mc Connell, Journal of Solid State Chemistry 34 (1980) 315–322.

[48] R.H. French, H. Müllejans, D.J. Jones, Journal of the American Ceramic Society 81 (1998) 2549–2557.

[49] V. Edlmayr, T.P. Harzer, R. Hoffmann, D. Kiener, C. Scheu, C. Mitterer, J. Vac. Sci. Technol. A 29 (2011) 41506–8.

[50] V. Edlmayr, M. Moser, C. Walter, C. Mitterer, Surface and Coatings Technology 204 (2010) 1576–1581.

[51] J.M. McHale, A. Auroux, A.J. Perrotta, A. Navrotsky, Science 277 (1997) 788–791.

[52] M.R. Gallas, B. Hockey, A. Pechenik, G.J. Piermarini, Journal of the American Ceramic Society 77 (1994) 2107–2112.

[53] P. Jin, G. Xu, M. Tazawa, K. Yoshimura, D. Music, J. Alami, U. Helmersson, J. Vac. Sci. Technol. A 20 (2002) 2134–2136.

[54] J.M. Andersson, E. Wallin, U. Helmersson, U. Kreissig, E.P. Münger, Thin Solid Films 513 (2006) 57–59.

[55] Y. Yamada-Takamura, F. Koch, H. Maier, H. Bolt, Proceedings of the 7th International Conference on Plasma Surface Engineering 142–144 (2001) 260–264.

[56] S. Ruppi, J. Phys. IV France 11 (2001) Pr3-847-Pr3-859.

[57] J. Musil, J. Blažek, P. Zeman, Š. Prokšová, M. Šašek, R. Čerstvý, Applied Surface Science 257 (2010) 1058–1062.

[58] R. Brill, F. Koch, J. Mazurelle, D. Levchuk, M. Balden, Y. Yamada-Takamura, H. Maier, H. Bolt, Proceedings of the Eight International Conference on Plasma Surface Engineering 174–175 (2003) 606–610.

[59] J. Rosen, S. Mraz, U. Kreissig, D. Music, J. Schneider, Plasma Chemistry and Plasma Processing 25 (2005) 303–317.

[60] P. Eklund, M. Sridharan, G. Singh, J. Bøttiger, Plasma Processes and Polymers 6 (2009) S907-S911.

[61] J.D. Cawley, J.W. Halloran, Journal of the American Ceramic Society 69 (1986) C-195.

[62] B.A. Pint, J.R. Martin, L.W. Hobbs, Solid State Ionics 78 (1995) 99–107.

[63] P.A. van Manen, E.W.A. Young, D. Schalkoord, C.J. van der Wekken, J.H.W. de Wit, Surf. Interface Anal. 12 (1988) 391–396.

[64] I. Rommerskirchen, V. Kolarik, Materials and Corrosion 47 (1996) 625–630.

[65] D.P. Moon, Materials Science and Technology 5 (1989) 754–764.

[66] J. Jedliński, Oxidation of Metals 39 (1993) 55–60.

[67] R.K. Iler, Journal of the American Ceramic Society 47 (1964) 339–341.

[68] M.S.J. Gani, R. McPherson, Journal of Materials Science 12 (1977) 999–1009.

[69] B. Yoldas, Journal of Materials Science 11 (1976) 465–470.

[70] C. Gerardin, S. Sundaresan, J. Benziger, A. Navrotsky, Chemistry of Materials 6 (1994) 160–170.

[71] C.-S. Hsi, H.-Y. Lu, F.-S. Yen, Journal of the American Ceramic Society 72 (1989) 2208–2210.

[72] E. Tkalcec, S. Kurajica, H. Ivankovic, Journal of the European Ceramic Society 25 (2005) 613–626.

[73] K. Okada, N. Ōtsuka, Journal of the American Ceramic Society 69 (1986) 652–656.

[74] D.W. Hoffman, R. Roy, S. Komarneni, Journal of the American Ceramic Society 67 (1984) 468–471.

[75] A.K. Chakraborty, Journal of the American Ceramic Society 88 (2005) 134–140.

[76] A.K. Chakraborty, Journal of Materials Science 43 (2008) 5313–5324.

[77] I.W.M. Brown, K.J.D. MacKenzie, M.E. Bowden, R.H. Meinhold, Journal of the American Ceramic Society 68 (1985) 298–301.

[78] W.-C. Wei, J.W. Halloran, Journal of the American Ceramic Society 71 (1988) 166–172.

[79] F. Maglia, S. Gennari, V. Buscaglia, Journal of the American Ceramic Society 91 (2008) 283–290.

[80] P. Hohenberg, W. Kohn, Phys. Rev. 136 (1964) B864.

[81] G. Kresse, J. Hafner, Phys. Rev. B 48 (1993) 13115–13118.

[82] J.P. Perdew, Y. Wang, Phys. Rev. B 46 (1992) 12947–12954.

[83] N.D.M. Hine, K. Frensch, W.M.C. Foulkes, M.W. Finnis, Phys. Rev. B 79 (2009) 24112.

[84] G. Paglia, C.E. Buckley, A.L. Rohl, R.D. Hart, K. Winter, A.J. Studer, B.A. Hunter, J.V. Hanna, Chem. Mater. 16 (2003) 220–236.

[85] W.Y. Ching, J. Chen, P. Rulis, L. Ouyang, A. Misra, Journal of Materials Science 41 (2006) 5061–5067.

[86] H.P. Pinto, R.M. Nieminen, S.D. Elliott, Phys. Rev. B 70 (2004) 125402.

[87] M. Fuchs, M. Bockstedte, E. Pehlke, M. Scheffler, Phys. Rev. B 57 (1998) 2134–2145.

[88] Ian G. Brown, Review of Scientific Instruments 65 (1994) 3061–3081.

[89] A. Anders, S. Anders, B. Juttner, W. Botticher, H. Luck, G. Schroder, Plasma Science, IEEE Transactions on 20 (1992) 466–472.

[90] P. Siemroth, B. Schultrich, T. Schülke, Fourth International Conference on Plasma Surface Engineering 74–75, Part 1 (1995) 92–96.

[91] H.C. Miller, Plasma Science, IEEE Transactions on 13 (1985) 242–252.

[92] A. Anders, G.Y. Yushkov, J. Appl. Phys. 91 (2002) 4824.

[93] D.M. Sanders, A. Anders, Surface and Coatings Technology 133–134 (2000) 78–90.

[94] A. Atiser, S. Mràz, J.M. Schneider, Journal of Physics D: Applied Physics 42 (2009) 15202.

[95] W.D. Davis, H.C. Miller, J. Appl. Phys. 40 (1969) 2212–2221.

[96] B. Jüttner, Beitr. Plasmaphys. 19 (1979) 25–48.

[97] J.E. Daalder, Journal of Physics D: Applied Physics 9 (1976) 2379.

[98] R.L. Boxman, S. Goldsmith, Surface and Coatings Technology 52 (1992) 39–50.

[99] D.A. Karpov, Surface and Coatings Technology 96 (1997) 22–33.

[100] P. Debye, P. Scherrer, Physik. Z. 17 (1916) 277–283.

[101] P.H. Mayrhofer, D. Music, J.M. Schneider, Appl. Phys. Lett. 100 (2006) 094906.

[102] R. Rachbauer, E. Stergar, S. Massl, M. Moser, P.H. Mayrhofer, Scripta Materialia 61 (2009) 725–728.

[103] P.H. Mayrhofer, D. Music, J.M. Schneider, Appl. Phys. Lett. 88 (2006) 71922–3.

[104] F. Rovere, D. Music, S. Ershov, M. to Baben, H.-G. Fuss, P. H. Mayrhofer and J. M. Schneider, Journal of Physics D: Applied Physics 43 (2010) 35302.

[105] F. Adibi, I. Petrov, L. Hultman, U. Wahlstrom, T. Shimizu, D. McIntyre, J.E. Greene, J.-E. Sundgren, J. Appl. Phys. 69 (1991) 6437–6450.

[106] S.-D. Mo, W.Y. Ching, Phys. Rev. B 57 (1998) 15219–15228.

[107] S.-D. Mo, Y.-N. Xu, W.-Y. Ching, Journal of the American Ceramic Society 80 (1997) 1193–1197.

[108] B. Ealet, M.H. Elyakhloufi, E. Gillet, M. Ricci, Thin Solid Films 250 (1994) 92–100.

[109] R.H. French, Journal of the American Ceramic Society 73 (1990) 477–489.

[110] V. I. Anisimov, F. Aryasetiawan and A. I. Lichtenstein, Journal of Physics: Condensed Matter 9 (1997) 767.

[111] T.C. Chou, T.G. Nieh, Journal of the American Ceramic Society 74 (1991) 2270–2279.

[112] D.X. Li, W.J. Thomson, Journal of Materials Research 6 (1991) 819–824.

[113] F.S. Ohuchi, S. Ghose, M.H. Engelhard, D.R. Baer, American Mineralogist 91 (May-June) 740–746.

[114] C.D. Wagner, D.E. Passoja, H.F. Hillery, T.G. Kinisky, H.A. Six, W.T. Jansen, J.A. Taylor, Journal of Vacuum Science and Technology 21 (1982) 933–944.

[115] J.F. Moulder, W.F. Stickle, E.P. Sobel, K.D. Bomben, in: J. Chastian (Ed.), Handbook of X-ray Photoelectron Spectroscopy, Perkin Elmer, Minnesota, 1992.

[116] P.R. Anderson, W.E. Swartz, Inorganic Chemistry 13 (1974) 2293–2294.

[117] S. Wannaparhun, S. Seal, V. Desai, Applied Surface Science 185 (2002) 183–196.

[118] T. P. Nguyen, S. Lefrant, Journal of Physics: Condensed Matter 1 (1989) 5197.

[119] W.A.M. Aarnink, A. Weishaupt and A. van Silfhout, Applied Surface Science 45 (1990) 37–48.

[120] F. Nahif, D. Music, S. Mráz, M. to Baben and J. M. Schneider, Journal of Physics: Condensed Matter 25 (2013) 125502.

[121] B.A. Pint, L.W. Hobbs, Journal of The Electrochemical Society 141 (1994) 2443–2453.

[122] J.S. Abell, I.R. Harris, B. Cockayne, B. Lent, J Mater Sci 9 (1974) 527-537.

[123] Y. Waku, N. Nakagawa, T. Wakamoto, H. Ohtsubo, K. Shimizu, Y. Kohtoku, Journal of Materials Science 33 (1998) 4943-4951.

[124] S. Lartigue-Korinek, C. Carry, L. Priester, Journal of the European Ceramic Society 22 (2002) 1525–1541.

[125] S. Galmarini, U. Aschauer, P. Bowen, S.C. Parker, Journal of the American Ceramic Society 91 (2008) 3643–3651.

[126] Y.J. Su, R.W. Trice, K.T. Faber, H. Wang, W.D. Porter, Oxidation of Metals 61 (2004) 253–271.

[127] J. Lu, K.-i. Ueda, H. Yagi, T. Yanagitani, Y. Akiyama, A.A. Kaminskii, Proceedings of the 5th International Conference on Excited States of Transition Elements 341 (2002) 220–225.

[128] A. Ikesue, K. Kamata, K. Yoshida, Journal of the American Ceramic Society 79 (1996) 1921–1926.

[129] T. Yanagida, H. Takahashi, T. Ito, D. Kasama, T. Enoto, M. Sato, S. Hirakuri, M. Kokubun, K. Makishima, T. Yanagitani, H. Yagi, T. Shigeta, Nuclear Science, IEEE Transactions on 52 (2005) 1836–1841.

[130] Y. Harada, N. Uekawa, T. Kojima, K. Kakegawa, Advances in Applied Ceramics 108 (2009) 78–83.

[131] W.P. Trower (Ed.), Cerium-doped yttrium aluminum perovskite (YAP): properties of commercial crystals, Cambridge Univ Press, 1994.

[132] S. Baccaro, K. Blažek, F. de Notaristefani, P. Maly, J.A. Mares, R. Pani, R. Pellegrini, A. Soluri, Nuclear Instruments and Methods in Physics Research Section A: Accelerators, Spectrometers, Detectors and Associated Equipment 361 (1995) 209–215.

[133] C. Pedrini, D. Bouttet, C. Dujardin, B. Moine, I. Dafinei, P. Lecoq, M. Koselja, K. Blazek, Optical Materials 3 (1994) 81–88.

[134] M. Veith, S. Mathur, A. Kareiva, M. Jilavi, M. Zimmer, V. Huch, J. Mater. Chem. 9 (1999) 3069–3079.

[135] Y. Liu, Z.-F. Zhang, B. King, J. Halloran, R.M. Laine, Journal of the American Ceramic Society 79 (1996) 385–394.

[136] C.J. Harlan, A. Kareiva, B. MacQueen, R. Cook, A.R. Barror, Adv. Mater. 9 (1997) 68–71.

[137] A. Ikesue, T. Kinoshita, K. Kamata, K. Yoshida, Journal of the American Ceramic Society 78 (1995) 1033–1040.

[138] J.-M. Yang, S.M. Jeng, S. Chang, Journal of the American Ceramic Society 79 (1996) 1218–1222.

[139] E. de La Rosa, La Diaz-Torres, P. Salas, A. Arredondo, J.A. Montoya, C. Angeles, R.A. Rodriguez, Optical Materials 27 (2005) 1793–1799.

[140] H. Kozuka, M. Kajimura, Journal of the American Ceramic Society 83 (2000) 1056–1062.

[141] Y. Deng, J.D. Fowlkes, P.D. Rack, J.M. Fitz-Gerald, Optical Materials 29 (2006) 183–191.

[142] G.-R. Bai, H.L.M. Chang, C.M. Foster, Applied Physics Letters 64 (1994) 1777–1779.

[143] F. Nahif, D. Music, S. Mráz, H. Bolvardi, L. Conrads, J.M. Schneider, Surface and Coatings Technology 235 (2013) 250–258.

[144] M.A. Gülgün, V. Putlayev, M. Rühle, Journal of the American Ceramic Society 82 (1999) 1849–1856.

[145] M.A. Gülgün, R. Voytovych, I. MacLaren, M. Rühle, R.M. Cannon, Interface Science 10 (2002) 99-110.

[146] R. Lach, K. Haberko , M. Bućko, Processing and Application of Ceramics 5 (2011) 187–191.

[147] W.Q. Li, L. Gao, Nanostructured Materials 11 (1999) 1073–1080.

Curriculum Vitae

Personal Details:

Name:	Farwah Nahif
Date of Birth:	15.10.1978
Born in:	Kabul/Afghanistan
Nationality:	German

Work:

07/2009 – 12/2009	Special Scientist at Nanotechnology Research Center Department of Mechanical and Manufacturing Engineering, University of Cyprus, Cyprus

Educational Qualification:

02/2010 – present	PhD student and research assistant at Lehrstuhl für Werkstoffchemie (MCh), RWTH Aachen University, Germany
10/2005 – 06/2009	Metallurgical & Materials Engineering, diploma studies at RWTH Aachen University, Germany Degree: Diploma (Dipl.-Ing.)
10/2000 – 10/2005	Mechanical Engineering, diploma studies at RWTH University, Germany
10/1998 – 04/2000	Traffic Engineering, diploma studies at Technische Universität Berlin, Germany
1989 – 1998	Secondary school: Kardinal-Frings-Gymnasium, Bonn-Beuel, Germany Degree: Certificate of General University Maturity